ADVANCED QUANTUM TECHNOLOGIES
www.advquantumtech.com

Generation of Non-Classical Light Using Semiconductor Quantum Dots

*Rahul Trivedi, Kevin A. Fischer, Jelena Vučković, and Kai Müller**

Sources of non-classical light are of paramount importance for future applications in quantum science and technology such as quantum communication, quantum computation and simulation, quantum sensing, and quantum metrology. This Review is focused on the fundamentals and recent progress in the generation of single photons, entangled photon pairs, and photonic cluster states using semiconductor quantum dots. Specific fundamentals which are discussed are a detailed quantum description of light, properties of semiconductor quantum dots, and light–matter interactions. This includes a framework for the dynamic modeling of non-classical light generation and two-photon interference. Recent progress is discussed in the generation of non-classical light for off-chip applications as well as implementations for scalable on-chip integration.

1. Introduction

Non-classical states of light such as single photons and entangled photons are key ingredients for photonic quantum technologies with applications in quantum communication, quantum computation, quantum simulation, quantum sensing, and quantum metrology.[1–9] Over the last two decades, semiconductor quantum dots (QDs) have established themselves as a very promising material platform for sources of such non-classical light.[10] This results from their strong interband transitions with near-unity quantum efficiency, almost exclusive emission into the zero phonon line (ZPL) and nearly transform-limited linewidth.[11–14] Moreover, the used III–V semiconductor materials allow to embed the QDs into optoelectronic devices which allows to electrically control the properties of the QDs, such as the emission wavelength.[15] Fabricating nanophotonic structures such as resonators and waveguides around QDs allows to further enhance the light–matter interaction in order to speed-up operational rates and to efficiently collect the generated non-classical light off-chip or route it on-chip for integrated quantum photonic circuits.[16] For example, a solitary high-quality QD source was recently used in exciting demonstrations to create a train of single photons, which were temporally multiplexed to the input of a boson sampler.[17,18]

Several books have already been written about semiconductor QDs[10] and multiple useful Reviews have recently been published, for example, on the generation of single photons,[19,20] entangled photon pairs,[21,22] or interfacing QDs with photonic nanostructures.[23,24] The Review here combines a comprehensive presentation of the quantum optical theory necessary to describe and understand the genesis of non-classical light-states in these systems with a summary of experimental realizations across a wide variety of state-of-the-art platforms. In Section 2, we will discuss all relevant fundamentals, including a thorough quantum optical description of light and the light–matter interaction. This also includes a framework that can be used to simulate the quantum optical properties of non-classical light generated by many different schemes. Then, in Sections 3–6, we review the recent progress in the generation of single photons, entangled photon pairs, and cluster states using semiconductor QDs. The recent developments strongly support the potential of QDs for applications in quantum communication and photonic quantum simulation.

2. Fundamentals

2.1. Quantum Description of Light

A full quantum treatment of electromagnetic fields forms the basis of describing the light produced by quantum emitters such as QDs. Quantization of an electromagnetic field can be performed by applying the second quantization principle to the classical Maxwell's equations. In the quantum description of the state of light, the electric field at each point $\mathbf{x}$ in space is treated as an observable whose statistics are captured by a Hermitian operator $\hat{\mathbf{E}}(\mathbf{x})$. The dynamics of the electromagnetic fields are described by a Hamiltonian $\hat{H}$, and the electromagnetic fields satisfy Schrodinger's equation with this Hamiltonian. Below,

R. Trivedi, Dr. K. A. Fischer, Prof. J. Vučković
E. L. Ginzton Laboratory
Stanford University
Stanford, CA 94305, USA
Prof. K. Müller
Walter Schottky Institut
Department of Electrical and Computer Engineering and MCQST
Technische Universität München
85748 Garching, Germany
E-mail: kai.mueller@wsi.tum.de

The ORCID identification number(s) for the author(s) of this article can be found under https://doi.org/10.1002/qute.201900007

DOI: 10.1002/qute.201900007

we provide expressions for the electric field operator $\hat{\mathbf{E}}(\mathbf{x})$ and the Hamiltonian $\hat{H}$ for a single-mode cavity and a single-mode waveguide (refer to Appendix A for a detailed derivation).

2.1.1. Single Mode Cavity

A lossless single-mode cavity can be described completely by its mode frequency ω_C and the mode field profile $\mathbf{E}_C(\mathbf{x})$. This mode has an annihilation operator a which satisfies the commutation $[\hat{a}, \hat{a}^\dagger] = 1$. The Hamiltonian for the single mode cavity reduces to $H = \omega_C \hat{a}^\dagger \hat{a}$ and the electric field operator can be expressed as

$$\hat{\mathbf{E}}(\mathbf{x}) = \left[\frac{\hbar\omega_C}{2\varepsilon_0 \int_\Omega \varepsilon(\mathbf{x})|\mathbf{E}_C(\mathbf{x})|^2 \mathrm{d}^3\mathbf{x}}\right]^{1/2} \mathbf{E}_C(\mathbf{x})\hat{a} + \text{h.c.} \tag{1}$$

where Ω refers to the interior of the cavity.

2.1.2. Lossy Cavities

Practically, optical cavities are unable to confine light perfectly, and suffer from absorption and radiation loss. While it is possible to derive the quantum description for such systems from first principles,[25] it is often sufficient to consider a heuristic model of this loss in which the cavity mode interacts with a continuum of harmonic oscillator modes, often referred to as the bath modes. More specifically, a lossy cavity can be described with the following Hamiltonian:

$$\hat{H} = \hbar\omega_C \hat{a}^\dagger \hat{a} + \int_0^\infty \hbar\omega \hat{b}^\dagger(\omega)\hat{b}(\omega)\mathrm{d}\omega + \hbar \int_0^\infty \xi(\omega)[\hat{b}(\omega)\hat{a}^\dagger + \hat{a}\hat{b}^\dagger(\omega)]\mathrm{d}\omega \tag{2}$$

where $b(\omega)$ is the annihilation operator for a bath mode at frequency ω, and satisfies the commutation relations $[\hat{b}(\omega), \hat{b}^\dagger(\omega')] = \delta(\omega - \omega')$ and $[\hat{b}(\omega), \hat{b}(\omega')] = 0$. Since the bath is a continuum of modes, decay of the cavity into it is irreversible which is consistent with what might be expected in a lossy cavity. Moreover, within the Markovian approximation (i.e., $\xi(\omega)$ being a constant ξ), it can be shown that in the Heisenberg picture, the operator $a(t)$ satisfies the following dynamical equation:[26]

$$\frac{\mathrm{d}a(t)}{\mathrm{d}t} = -\left(\mathrm{i}\omega_c + \frac{\kappa}{2}\right)a(t) - \mathrm{i}\sqrt{\kappa}\eta(t) \tag{3}$$

where $\kappa = 2\pi\xi^2$ is the decay rate of the cavity (related to its quality factor Q by $\kappa = \omega_0/Q$), and $\eta(t)$ is an operator acting on the bath modes that annihilates its vacuum state ($\eta(t)|\text{vac}\rangle = 0$) and satisfies the commutation relations $[\eta(t), \eta^\dagger(t')] = \delta(t - t')$, $[\eta(t), \eta(t')] = 0$. From Equation (3), we clearly see that the cavity mode operator decays exponentially with time as would be expected in a lossy cavity. However, in addition to the exponential decay, we also have an input term $\eta(t)$—this input term models the impact of vacuum fluctuations in the bath modes on the dynamics of the cavity.

Rahul Trivedi graduated from the Indian Institute of Technology Delhi in 2016 with a B.Tech in Electrical Engineering. He is currently working toward a Ph.D. in Electrical Engineering at Stanford University, CA, USA. His work focusses on theoretical and computational aspects of nanophotonics and quantum optics.

Jelena Vuckovic (Ph.D. Caltech 2002) is a Jensen Huang Professor in Global Leadership in the Stanford School of Engineering and Professor by courtesy of Applied Physics at Stanford. She is also the director of the Q-FARM: the Stanford-SLAC Quantum Initiative. She is a Fellow of APS, OSA, and IEEE, and a Distinguished Fellow of the Max Planck Institute for Quantum Optics.

Kai Müller is professor for Quantum Electronics and Computer Engineering at the Technical University of Munich (TUM), Germany. His current research is focused on the development of building blocks for modular photonic quantum technologies as well as fully integrated quantum-photonic circuits. After completing a Ph.D. in physics at TUM, he worked as a postdoctoral researcher at Stanford University. Subsequently, he established a junior research group at the Walter Schottky Institute of TUM. Since 2019, he is an assistant professor in the Department of Electrical and Computer Engineering of TUM.

2.1.3. Single-Mode Waveguides

The propagation of light within a single-mode waveguide can be described completely by a continuum of modes indexed by the wavenumber β, a dispersion relationship indicating the frequency $\omega(\beta)$ of the propagating modes and their mode profiles $\mathbf{E}(\mathbf{x}; \beta)$—assuming that the propagation axis is x and $\boldsymbol{\rho}$ denotes the transverse coordinate, this mode has the form $\mathbf{E}(\boldsymbol{\rho}; \beta)\exp(\mathrm{i}\beta x)$. Each mode has an associated annihilation operator $\hat{a}(\beta)$, which satisfies the commutator $[\hat{a}(\beta), \hat{a}^\dagger(\beta')] = \delta(\beta - \beta')$ and $[\hat{a}(\beta), \hat{a}(\beta')] = 0$. The Hamiltonian for the single-mode

waveguide reduces to

$$\hat{H} = \int_0^\infty \hbar\omega(\beta)\hat{a}^\dagger(\beta)\hat{a}(\beta)\mathrm{d}\beta \tag{4}$$

with the electric field operator being given by

$$\hat{\mathbf{E}}(\mathbf{x}) = \int_0^\infty \left[\frac{\hbar\omega(\beta)}{2\varepsilon_0\int_\Gamma \varepsilon(\boldsymbol{\rho})|\mathbf{E}(\boldsymbol{\rho};\beta)|^2\mathrm{d}^2\boldsymbol{\rho}}\right]^{1/2} \times \mathbf{E}(\boldsymbol{\rho};\beta)\exp(\mathrm{i}\beta x)\hat{a}(\beta)\mathrm{d}\beta + \mathrm{h.c.} \tag{5}$$

where we have assumed the waveguide mode to support propagation in only one direction and Γ is the cross section of the waveguide. Note that propagation in the backward direction can be modeled as another single-mode waveguide. We note that unlike the description for a lossless cavity, a model for a waveguide mode requires a definition of an annihilation operator for a continuum of frequencies or propagation constants. This is a consequence of the waveguide not confining light in all three dimensions. Alternatively, defining the annihilation operator in terms of frequency ω instead of the propagation constant, $\hat{a}(\omega) = \hat{a}(\beta(\omega))/\sqrt{v_G(\omega)}$ (where $v_G(\omega)$ is the group velocity of the waveguide mode at frequency ω), which has commutation relations $[\hat{a}(\omega), \hat{a}^\dagger(\omega')] = \delta(\omega-\omega')$ and $[\hat{a}(\omega), \hat{a}(\omega')] = 0$, the Hamiltonian can be expressed as

$$\hat{H} = \int_{\omega_c}^\infty \hbar\omega\hat{a}^\dagger(\omega)\hat{a}(\omega)\mathrm{d}\omega \tag{6}$$

where ω_c is the cut-off frequency of the waveguide mode, and the electric field operator can be expressed as

$$\hat{\mathbf{E}}(\mathbf{x}) = \int_{\omega_c}^\infty \left[\frac{\hbar\omega}{2\varepsilon_0 v_G(\omega)\int_\Gamma \varepsilon(\boldsymbol{\rho})|\mathbf{E}(\boldsymbol{\rho};\beta(\omega))|^2\mathrm{d}^2\boldsymbol{\rho}}\right]^{1/2} \times \mathbf{E}(\boldsymbol{\rho};\omega)\exp[\mathrm{i}\beta(\omega)x]\hat{a}(\omega)\mathrm{d}\omega + \mathrm{h.c.} \tag{7}$$

Finally, we note well collimated free-space optical modes such as Gaussian beams can also be modeled similar to the waveguide mode, with one annihilation operator $\hat{a}(\omega)$ associated with each frequency propagating in the Gaussian beam.

2.2. Quantum States of Light

Light emission from sources of quantum light are fundamentally collected into a waveguide mode or a propagating beam—additionally, since a waveguide mode or a propagating beam can support a continuum of frequencies, such states are fundamentally multimode states. In this section, we provide an overview of the theoretical description of such states, as well as some metrics to quantify their properties.

Consider a quantum light source emitting light into L bosonic loss channels with annihilation operators $\hat{a}_\mu(\omega),\ \mu \in \{1, 2 \dots L\}$. These different bosonic loss channels physically correspond to independent propagating modes—examples of such modes would be modes with different polarizations, different modes of a multimode waveguide or fiber or modes of physically different waveguides. In general, an N-photon state $|\psi^{(N)}\rangle$ in the loss channel can be described by an N-body bosonic wavefunction $\psi_{\mu_1,\mu_2\dots\mu_N}(\omega_1,\omega_2\dots\omega_N)$:

$$|\Psi^{(N)}\rangle = \frac{1}{\sqrt{N!}}\sum_{\mu_1\dots\mu_N=1}^{L}\int_{-\infty}^{\infty}\int_{-\infty}^{\infty}\cdots\int_{-\infty}^{\infty}\psi^{(N)}_{\mu_1,\mu_2\dots\mu_N}(\omega_1,\omega_2\dots\omega_N) \times\prod_{i=1}^{N}\hat{a}^\dagger_{\mu_i}(\omega_i)\mathrm{d}\omega_i|\mathrm{vac}\rangle \tag{8}$$

where $\psi^{(N)}_{\mu_1,\mu_2\dots\mu_N}(\omega_1,\omega_2\dots\omega_N)$ is symmetric with respect to a simultaneous permutation of ω_i and μ_i and we integrate over the frequencies from $-\infty$ to ∞ with the understanding that the wavefunction is zero at frequencies that cannot propagate in the optical mode under consideration (e.g., frequencies that are below the cut-off frequency of a waveguide). Note that $\hat{a}_\mu(\omega)$ is the annihilation operator corresponding to field propagating at frequency ω in the μth losschannel and satisfies the commutation relations $[\hat{a}_\mu(\omega), \hat{a}_{\mu'}(\omega')] = 0, [\hat{a}_\mu(\omega), \hat{a}^\dagger_{\mu'}(\omega')] = \delta_{\mu,\mu'}\delta(\omega-\omega')$. Furthermore, the N-body wavefunction $\psi_{\mu_1,\mu_2\dots\mu_N}(\omega_1,\omega_2\dots\omega_N)$ satisfies the normalization condition

$$\sum_{\mu_1\dots\mu_N=1}^{L}\int_{-\infty}^{\infty}\int_{-\infty}^{\infty}\cdots\int_{-\infty}^{\infty}|\psi^{(N)}_{\mu_1,\mu_2\dots\mu_N}(\omega_1,\omega_2\dots\omega_N)|^2 \times\mathrm{d}\omega_1\mathrm{d}\omega_2\dots\mathrm{d}\omega_N = 1 \tag{9}$$

An alternative way of expressing the state of the light in a loss channel is by using the "position" annihilation operator $\hat{a}_\mu(x)$, which is defined as the inverse Fourier transform of the operator $\hat{a}(\omega)$:

$$\hat{a}_\mu(x) = \int_{-\infty}^{\infty}\hat{a}_\mu(\omega)\exp\left(\frac{\mathrm{i}\omega x}{v_G}\right)\frac{\mathrm{d}\omega}{\sqrt{2\pi v_G}} \tag{10}$$

$\hat{a}_\mu(x)$ $[\hat{a}^\dagger_\mu(x)]$ can be considered to annihilate (create) a photon at a position x along the propagation direction of the optical mode and v_G is the group velocity of the optical mode under consideration. The commutation relationship for $\hat{a}_\mu(\omega)$ imply that $[\hat{a}_\mu(x), \hat{a}_\mu(x')] = 0$ and $[\hat{a}_\mu(x), \hat{a}^\dagger_{\mu'}(x')] = \delta_{\mu,\mu'}\delta(x-x')$. The N-photon state as defined in Equation (8) can be rewritten in terms of the position operator to obtain

$$|\Psi^{(N)}\rangle = \frac{1}{\sqrt{N!}}\sum_{\mu_1\dots\mu_N=1}^{L}\int_{-\infty}^{\infty}\int_{-\infty}^{\infty}\cdots\int_{-\infty}^{\infty}\psi^{(N)}_{\mu_1,\mu_2\dots\mu_N}(x_1,x_2\dots x_N) \times\prod_{i=1}^{N}\hat{a}^\dagger_{\mu_i}(x_i)\mathrm{d}x_i|\mathrm{vac}\rangle \tag{11}$$

where $\psi^{(N)}_{\mu_1,\mu_2\dots\mu_N}(x_1,x_2\dots x_N)$, the amplitude of finding the N-photons at $x_1, x_2 \dots x_N$, is related to $\psi^{(N)}_{\mu_1,\mu_2\dots\mu_N}(\omega_1,\omega_2\dots\omega_N)$ via an inverse Fourier transform:

$$\psi^{(N)}_{\mu_1,\mu_2\dots\mu_N}(x_1,x_2\dots x_N) = \int_{-\infty}^{\infty}\int_{-\infty}^{\infty}\cdots\int_{-\infty}^{\infty}\psi^{(N)}_{\mu_1,\mu_2\dots\mu_N}(\omega_1,\omega_2\dots\omega_N) \times\prod_{i=1}^{N}\exp\left(\frac{\mathrm{i}\omega_i x_i}{v_G}\right)\frac{\mathrm{d}\omega_i}{\sqrt{2\pi v_G}} \tag{12}$$

In the position basis representation for the N-photon state, its time evolution under the Hamiltonian (Equation (6)) is equivalent to translating the $\psi^{(N)}_{\mu_1,\mu_2\ldots\mu_N}(x_1, x_2 \ldots x_N)$ along every coordinate by the elapsed time. More explicitly

$$\exp(-\mathrm{i}Ht)\left|\Psi^{(N)}\right\rangle = \frac{1}{\sqrt{N!}}\sum_{\mu_1\ldots\mu_N=1}^{L}\int_{-\infty}^{\infty}\int_{-\infty}^{\infty}\cdots\int_{-\infty}^{\infty}$$

$$\psi_{\mu_1,\mu_2\ldots\mu_N}(x_1 + v_G t, x_2 + v_G t \ldots x_N + v_G t)\prod_{i=1}^{N}\hat{a}^{\dagger}_{\mu_i}(x_i)\mathrm{d}x_i|\mathrm{vac}\rangle \quad (13)$$

which follows directly from Equation (6), the definition of $\hat{a}_{\mu}(x)$, and the commutators for $\hat{a}_{\mu}(\omega)$—this intuitively corresponds to the light propagating down the loss channel with velocity v_G. The set of states $\{|\Psi^{(k)}\rangle\ \forall\ k \in \{0, 1, 2\ldots\}\}$ forms a complete basis for the Hilbert space of the loss channel. The light emitted by quantum light sources into a loss channel can therefore be expressed as a superposition of such states:

$$|\Psi\rangle = \sqrt{P_0}|\mathrm{vac}\rangle + \sum_{i=1}^{\infty}\sqrt{P_i}\left|\Psi^{(i)}\right\rangle \quad (14)$$

where P_i is the probability that the emitted light has i photons ($P_0 + P_1 + P_2 + \cdots = 1$).

2.2.1. Light Emitted by Single-Photon Sources

Of special interest are the states emitted by a single-photon source, and a coherent source. A *single-photon* source coupling only to a single loss channel would emit a state given by

$$|\Psi\rangle = \sqrt{P_0}|\mathrm{vac}\rangle + \sqrt{P_1}\left|\Psi^{(1)}\right\rangle \quad (15)$$

with $P_0 + P_1 = 1$. P_1 is the probability that a single-photon emission has happened, it is therefore desirable to make P_1 as large as possible. An important consideration here is that while most single photon sources invariably couple to multiple loss channels—which may include loss channels that correspond to radiation or absorption losses in the source—light collection from the source happens through only one of them. In such cases, the state of light in the output loss channel can no longer be described by a pure state but rather by a density matrix $\hat{\rho}$ which is obtained by tracing over the loss channels that are not collected at the output. Assuming that the source only emits a single photon, $\hat{\rho}$ has the form

$$\hat{\rho} = P_0|\mathrm{vac}\rangle\langle\mathrm{vac}| + P_1\hat{\rho}^{(1)} + \hat{\rho}^{(\chi)} \quad (16)$$

where $P_0 + P_1 = 1$ and

$$\hat{\rho}^{(\chi)} = \int_{-\infty}^{\infty}\left[\rho^{(\chi)}(\omega)\hat{a}^{\dagger}(\omega)|\mathrm{vac}\rangle\langle\mathrm{vac}| + \rho^{(\chi)*}(\omega)|\mathrm{vac}\rangle\langle\mathrm{vac}|\hat{a}(\omega)\right]\mathrm{d}\omega \quad (17)$$

$$\hat{\rho}^{(1)} = \int_{-\infty}^{\infty}\int_{-\infty}^{\infty}\rho^{(1)}(\omega_1, \omega_2)\hat{a}^{\dagger}(\omega_1)|\mathrm{vac}\rangle\langle\mathrm{vac}|\hat{a}(\omega_2)\mathrm{d}\omega_1\mathrm{d}\omega_2 \quad (18)$$

where $\rho^{(1)}(\omega_1, \omega_2) = \rho^{(1)*}(\omega_2, \omega_1)$ and the following normalization condition is satisfied:

$$\mathrm{Trace}(\hat{\rho}^{(1)}) = \int_{-\infty}^{\infty}\rho^{(1)}(\omega, \omega)\mathrm{d}\omega = 1 \quad (19)$$

We note that the $\hat{\rho}^{(1)}(\omega_1, \omega_2)$ describes the density matrix of the photon state within the single-photon subspace. If $\omega_1 \neq \omega_2$, then $\hat{\rho}^{(1)}(\omega_1, \omega_2)$ evaluates to the off-diagonal density matrix element between single-photon states at ω_1 and ω_2 and thus has information about the coherence between the photons at ω_1 and ω_2. If $\omega_1 = \omega_2$, then it simply provides information about the probability of detecting a photon at frequency $\omega_1 = \omega_2$ as a fraction of the total probability of detecting a single-photon (P_1). Similarly, $\hat{\rho}^{(\chi)}$ is the off-diagonal density matrix element between a photon at frequency ω and the vacuum state.

Note that if the emitted light is in a pure state (i.e., the source couples only to the output loss channel), then density matrix factorizes into a product of a bra and a ket: $\hat{\rho} = |\Psi\rangle\langle\Psi|$. In terms of $\hat{\rho}^{(\chi)}$ and $\hat{\rho}^{(1)}$, this is equivalent to $\rho^{(\chi)}(\omega) = \sqrt{P_0 P_1}\psi^{(1)}(\omega)$ and $\rho^{(1)}(\omega_1, \omega_2) = \psi^{(1)}(\omega_1)\psi^{(1)*}(\omega_2)$. For a more general mixed state, it is possible to express the density matrix as a sum of such factorizable terms:

$$\hat{\rho} = \sum_i \sigma_i|\Psi_i\rangle\langle\Psi_i| \quad (20)$$

where $1 \geq \sigma_1 \geq \sigma_2 \cdots \geq 0$, $\sigma_1 + \sigma_2 \cdots = 1$ and $\langle\Psi_i|\Psi_j\rangle = \delta_{i,j}$. This is referred to as the Schmidth decomposition[27] of the density matrix—physically, this decomposition can be interpreted as indicating that the state is in a mixture of pure states $|\Psi_i\rangle$, with the contribution of the ith pure state being σ_i. The rank of this decomposition (i.e., number of non-zeros or large σ_i) can be taken as an indicator of how "pure" the state is.

Below, we briefly define some metrics that can be used to characterize such a single-photon source:

1. *Spectral Content*: The spectral content $n(\omega)$ of a single photon source can be defined by the average number of photons per unit frequency emitted by the source at a given frequency. This can be computed by averaging the operator $\hat{a}^{\dagger}(\omega)\hat{a}(\omega)$ over the state of the emitted light:

$$n(\omega) = \mathrm{Trace}(\hat{\rho}\hat{a}^{\dagger}(\omega)\hat{a}(\omega)) = \mathrm{Trace}(\hat{a}(\omega)\hat{\rho}\hat{a}^{\dagger}(\omega)) = P_1\rho^{(1)}(\omega, \omega) \quad (21)$$

   For a source emitting a pure state, this further simplifies to $n(\omega) = P_1|\psi^{(1)}(\omega)|^2$.
2. *Brightness*: The brightness of the source can be defined as the average number of photons emitted by the source, that is, integrating $n(\omega)$ over all frequencies—this evaluates to P_1, which is also equal to the probability of the source emitting a single photon.
3. *Trace Purity*: The trace purity of the single photon source characterizes how close to a pure state is the emitted single photon state. Mathematically, it is defined by

$$\mathrm{Trace}(\hat{\rho}^2) = P_0^2 + 2\left|\int_{-\infty}^{\infty}\rho^{(\chi)}(\omega)\mathrm{d}\omega\right|^2 + P_1^2\int_{-\infty}^{\infty}\rho^{(1)}(\omega, \omega)\mathrm{d}\omega \quad (22)$$

For the emitted light being in a pure state, it can be readily verified that the trace purity evaluates to 1. A mixed state would have a trace purity smaller than 1, with its deviation from 1 signifying the extent to which it is not a pure state.[28]

2.2.2. N-Photon Fock States

While Equation (8) describes a general N-photon state, an N-photon Fock state is one in which all the photons are in exactly the same mode. For an N-photon Fock state propagating in waveguide mode with an annihilation operator $\hat{a}(\omega)$ in a mode with complex spectrum $\psi(\omega)$ is given by

$$|\psi^{(N)}\rangle = \frac{1}{\sqrt{N!}}\left[\int_{-\infty}^{\infty}\psi(\omega)\hat{a}^{\dagger}(\omega)\mathrm{d}\omega\right]^{N}|\mathrm{vac}\rangle \tag{23}$$

where $\psi(\omega)$ is normalized such that

$$\int_{-\infty}^{\infty}|\psi(\omega)|^2 = 1 \tag{24}$$

We note that this state corresponds to an N-photon state as described by Equation (8) propagating in a single loss channel with a separable many-body wavefunction, that is, $\psi(\omega_1, \omega_2 \ldots \omega_N) = \psi(\omega_1)\psi(\omega_2)\ldots\psi(\omega_N)$. This seperability of the wavefunction is a unique property of the N-photon Fock state, and not every $N-$photon state emitted from quantum states has this property. For instance, the two-photon state emitted by a two-level system after being excited by a short 2π pulse[29,30] is not a Fock state, that is, its two-body wavefunction is not separable. Fock states can also be constructed in the presence of multiple loss channels—an N photon Fock state with n_k photon in the loss channel μ_k ($N = n_1 + n_2 \ldots$) in a mode with the complex spectrum $\psi_k(\omega)$ is given by

$$|\psi^{(N)}\rangle = \prod_k \frac{1}{\sqrt{n_k!}}\left[\int_{-\infty}^{\infty}\psi_k(\omega)\hat{a}^{\dagger}_{\mu_k}(\omega)\mathrm{d}\omega\right]^{n_k}|\mathrm{vac}\rangle \tag{25}$$

We note that the normalization factor in the state when the Fock state is constructed in different loss channels is different from the normalization factor in the state when the Fock state is constructed in the same loss channel—this is a consequence of the Fock state in Equation (23) being composed entirely of identical single photons, whereas the Fock state in Equation (25) being composed of non-identical photons.

2.2.3. Coherent State

Another quantum state of interest is the *coherent state*, which is a model for the state of light emitted by a laser. This state of light is often used for driving non-classical light-sources—non-classical light-sources can thus often be considered to be systems that convert a coherent state into a non-classical state. A coherent state propagating in a waveguide mode with annihilation operator $\hat{a}(\omega)$ is defined by

$$\begin{aligned}|\alpha(\omega)\rangle &= \exp\left(\int_{-\infty}^{\infty}\left[\alpha(\omega)\hat{a}^{\dagger}(\omega) - \alpha^{*}(\omega)\hat{a}(\omega)\right]\mathrm{d}\omega\right)|\mathrm{vac}\rangle \\ &= \exp\left(-\frac{1}{2}\int_{-\infty}^{\infty}|\alpha(\omega)|^2\mathrm{d}\omega\right)\exp\left(\int_{-\infty}^{\infty}\alpha(\omega)\hat{a}^{\dagger}(\omega)\right)|\mathrm{vac}\rangle\end{aligned} \tag{26}$$

where $\alpha(\omega)$ is the complex spectrum of the coherent state—it provides information about the amplitude and phase of the light emitted from the laser at frequency ω. This state is a common eigenvector of the annihilation operator $\hat{a}(\omega)$ at all frequencies, satisfying the eigenvalue equation $\hat{a}(\omega)|\alpha(\omega)\rangle = \alpha(\omega)|\alpha(\omega)\rangle$. The mean photon number in such a coherent state is given by $\int|\alpha(\omega)|^2\mathrm{d}\omega$, and can be taken as a measure of the brightness of the state. Note that unlike the state emitted by a single-photon source, the mean photon number can be arbitrarily large if sufficient energy is put into the coherent state. The coherent state is regarded to be the closest approximation of a classical state of light within all possible quantum states.[31]

2.3. Semiconductor Quantum Dots

Optically active semiconductor QDs are nanometer-sized inclusions of a lower bandgap material embedded in a matrix of larger bandgap material.[33] This leads to a 3D confinement for electrons and holes with discrete shell-like energy levels which exhibit strong optical interband transitions (**Figure 1**a). These transitions have a near-unity quantum efficiency and almost exclusive emission into the ZPL which makes QDs ideal for sources of non-classical light. The energies of these transitions results from the bandgap, confinement energy, strain, and Coulomb interactions between the charge carriers.

Typically, QDs are grown by molecular beam epitaxy (MBE) or metalorganic chemical vapour deposition (MOCVD) and over the years different material combinations and growth techniques have been established. The most common QDs are InAs/GaAs QDs grown by strain-driven self-assembly (Stranski–Krastanov [SK] growth) where the lattice mismatch between InAs and GaAs leads to the formation of QDs after a certain critical thickness of InAs is reached. In this growth mode, the QDs form on top of a quantum well which is referred to as the wetting layer. Depending on the growth conditions, In(Ga)As/GaAs QDs typically emit in the range 900–1300 nm. To obtain InAs QDs emitting in the telecommunication C-band (1530–1565 nm) the lattice mismatch has to be reduced which can be achieved by using InP or AlGaInAs as the substrate.[34–36] In addition, it was recently demonstrated that metamorphic InGaAs strain-relaxation layers can also be used to shift the emission of InAs QDs into the C-band.[37] In addition to the SK growth, droplet epitaxy and droplet etching methods have been established which result in strain-free QDs. Here, demonstrated material combinations are GaAs/AlGaAs QDs emitting at 780 nm,[38–40] InAs/GaAs QDs emitting around 900 nm,[41] and InAs/InP QDs emitting at 1550 nm.[41] Also, pyramidal QDs grown in tetrahedral recesses etched in GaAs have recently demonstrated strong potential for

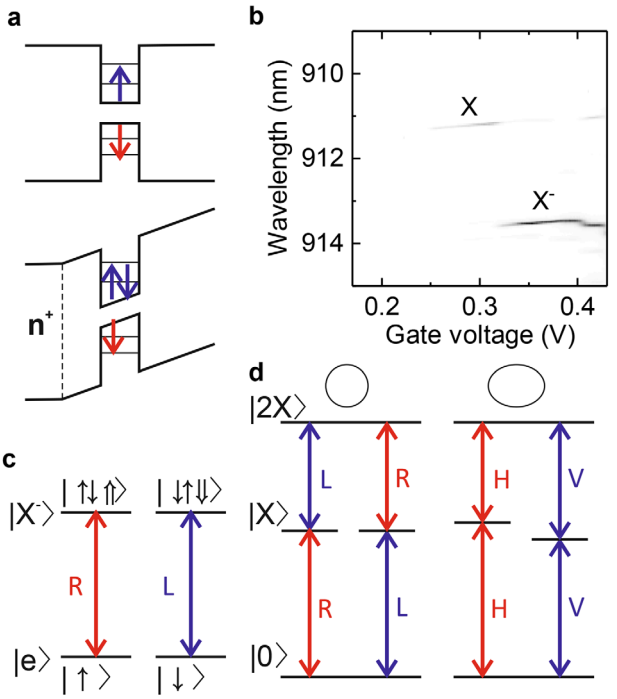

Figure 1. Semiconductor quantum dots. a) Schematic illustration of band structure in growth direction (top) without and (bottom) with applied electric field. b) Gate voltage dependent photoluminescence measurement illustrating the DC-Stark effect and sequential charging. c) Level scheme with optical transitions of a singly charged QD. d) Level scheme with optical transitions of an uncharged QD with (left) and without (right) D_{2D} symmetry. (b) Adapted under a Creative Commons Attribution 4.0 international license.[32] Copyright 2018, The Author, Published by Springer Nature.

scalable non-classical light sources.[42] A different method for growing QDs are nanowire-QDs where during the 1D growth of InP nanowires a InAsP segment is grown which forms a QD.[43]

Embedding QDs into diode structures (Figure 1a) allows to tune their emission energies via the DC-Stark effect. Moreover, carefully choosing the distance between QDs and an n-doped or p-doped reservoir allows to deterministically charge the QDs with electrons or holes.[15] If the lowest electron level in the QD is lowered below the Fermi energy the QD is deterministically charged with a single electron. Figure 1b shows a gate-voltage dependent photoluminescence measurement of a QD under non-resonant excitation and reveals clear stability plateaus which can be assigned to the charge neutral exciton X which consists of of one electron and one hole and a singly charged exciton X^- which consists of two electrons and one hole. In addition, embedding QDs into diode structures also stabilizes the electronic environment which reduces inhomogeneous broadening and allows for nearly transform-limited linewidth.[11,14] Further, residual frequency-shifts of the resonance can be actively compensated toward achieving transform-limited emission.[12,13]

In general, III–V semiconductors have one conduction band and three valence bands (heavy hole, light hole, split-off band). However, due to the large energy separation of the split-off band it does not play a role. Typically, QDs have a width of 20–50 nm and a height of 3–5 nm. In the growth direction, their band structure can be approximated as 1D quantum wells for electrons and holes where due to the large energy separation between the states only the lowest energy state plays a role. Moreover, quantum confinement and strain lift the heavy hole–light hole degeneracy such that except in structures which are strained on purpose[44] the highest energy conduction band states have predominant heavy hole character. Perpendicular to the growth direction the band structure can be approximated by a 2D harmonic oscillator leading to a shell-like energy structure for electrons and holes where similar to atoms the shells are labeled s-shell, p-shell, d-shell, and so on. This results in optical selection rules where transitions are only allowed if the conduction band and valence band states have the same parity.

Due to the confinement and strain, the lowest energy levels for holes have an angular momentum of $J_z = \pm\frac{3}{2}$ while electrons have a spin of $S_z = \pm\frac{1}{2}$. Therefore, each orbital state has a spin degeneracy of 2 and singly charged QDs exhibit two optical transitions which couple to right-handed and left-handed circularly polarized light (Figure 1c). The s-shell of uncharged QDs can host two electrons and two holes which is called the biexciton state and labeled 2X or XX (Figure 1d). Due to the Coulomb interaction and correlation effects in general, the transition X–2X has a different energy than the 0–X transition. For perfectly symmetric QDs, the two X states are degenerate and couple to 0 and 2X via circularly polarized light. Any deviation from this cylindrical symmetry due to strain, shape anisotropy, or random alloying lifts the degeneracy of the X states via the exchange interaction. The resulting energy gap, known as the fine-structure splitting, and the resulting linearly polarized selection rules are shown in Figure 1d.[45]

As a consequence, when resonantly exciting a neutral QD with a narrow-band laser the two X states can be addressed individually and treated as two-level systems. However, when exciting a neutral QD with short pulses which are spectrally broader than the FSS and where the polarization is different than H or V a coherent superposition of the two X states is created which precesses in time. This is particularly important for resonant spectroscopy where the excitation laser is typically suppressed from the QDs emission by using orthogonal linear polarizations for excitation and detection. Therefore, when exciting an uncharged QD with a short optical laser pulse the observed signal strongly depends on the choice of polarization relative to the QDs axis.[46] H or V polarized light will excite the QD in one of the two X states and since the emission has the same polarization it will be suppressed in the detection channel. On the other hand, exciting with a diagonal polarization will create a precessing superposition such that the orthogonally polarized detection channel will collect signal which oscillates in time.[47]

2.4. Light–Matter Interaction

Light–matter interactions lie at the heart of non-classical light generation—a full quantum treatment of the emitter and the optical field is required to model such interactions at the quantum level. Fundamentally, the interaction of an emitter with an electromagnetic field is due to its dipole moment—in the language of quantum mechanics, this dipole is described by an operator $\hat{\boldsymbol{\mu}} = -e\hat{\mathbf{x}}$ where $\hat{\mathbf{x}}$ is the operator corresponding to the difference

between the positions of positive and negative charge in the emitter. Denoting by $|g\rangle$ and $|e\rangle$ the two states between which an optical transition happens, this operator can be expressed as

$$\hat{\boldsymbol{\mu}} = \boldsymbol{\mu}\hat{\sigma} + \boldsymbol{\mu}^*\sigma^\dagger \tag{27}$$

where $\sigma = |g\rangle\langle e|$, $\sigma^\dagger = |e\rangle\langle g|$ and for simplicity we has assumed that $\langle e|\hat{\mathbf{x}}|e\rangle = \langle g|\hat{\mathbf{x}}|g\rangle = 0$. Since the variance in the position of electrons in the emitter is typically much smaller than the wavelength of light, the interaction Hamiltonian between the emitter and electromagnetic field can be approximated by[48]

$$\hat{H}_I = -\hat{\boldsymbol{\mu}} \cdot \hat{\mathbf{E}}(\mathbf{x}_D) \tag{28}$$

where $\hat{\mathbf{E}}(\mathbf{x}_D)$ is the electric field operator at the (mean) position $\mathbf{x}_D$ of the emitter's dipole. The dynamics of an emitter emerging from such an interaction Hamiltonian can have vastly different characteristics depending on the electromagnetic structure. For example, using this Hamiltonian to study the dynamics of an emitter coupling to bulk homogenous media, the phenomenon of spontaneous emission and Lamb shifts in the emitter frequency have been successfully explained.[48] Moreover, coupling emitters to optical cavities and waveguides allow for an engineering of spontaneous emission rates by controlling their quality factors and the dispersion relations, respectively. Additionally, coupling emitters to waveguides or emitters to cavities which emit into waveguides is a potential strategy for achieving a high collection efficiency of the photons emitted from the emitters into a well defined optical mode which can then be routed to various quantum information processing blocks. Below, we briefly review the basic dynamics of emitters coupling to optical cavities and waveguides.

2.4.1. Emitters Coupling to Cavities

In this case, the interaction Hamiltonian simplifies to

$$\hat{H}_I = g\sigma^\dagger a + f\sigma a + \text{h.c.} \tag{29}$$

where

$$g = -\left[\frac{\hbar\omega_C}{2\varepsilon_0\int_\Omega \varepsilon(\mathbf{x})|\mathbf{E}_C(\mathbf{x})|^2 \mathrm{d}^3\mathbf{x}}\right]^{1/2} \boldsymbol{\mu}^* \cdot \mathbf{E}_C(\mathbf{x}_D) \text{ and}$$

$$f = -\left[\frac{\hbar\omega_C}{2\varepsilon_0\int_\Omega \varepsilon(\mathbf{x})|\mathbf{E}_C(\mathbf{x})|^2 \mathrm{d}^3\mathbf{x}}\right]^{1/2} \boldsymbol{\mu} \cdot \mathbf{E}_C(\mathbf{x}_D) \tag{30}$$

Note that the interaction Hamiltonian $\hat{H}_I$ has terms that correspond to the simultaneous creation (annihilation) of a photon and excitation (decay) of the emitter to its excited state (ground state)—$\hat{a}^\dagger\hat{\sigma}^\dagger$ ($\hat{a}\hat{\sigma}$). This term produces extremely high-frequency contribution ($\approx \omega_C + \omega_E$, where ω_E is the frequency corresponding to the transition energy of the emitter) to the evolution of the system—if $|f|, |g| \ll \omega_C, \omega_E$, then the contribution of such terms to the interaction Hamiltonian can be ignored:

$$\hat{H}_I \approx g\sigma a^\dagger + g^* a\sigma^\dagger \tag{31}$$

This approximation is often called the rotating wave approximation—the resulting Hamiltonian, called the Jaynes–Cummings interaction Hamiltonian, lies at the heart of cavity quantum electrodynamics. The coupling constant g, which governs the strength of the cavity–emitter interaction, depends on the position of the dipole and how well the cavity mode is confined. By defining the mode volume V_M of the cavity by

$$V_M = \frac{\int_\Omega \varepsilon(\mathbf{x})|\mathbf{E}_C(\mathbf{x})|^2 \mathrm{d}^3\mathbf{x}}{\max[\varepsilon(\mathbf{x})|\mathbf{E}_C(\mathbf{x})|^2]} \tag{32}$$

This coupling constant can be re-expressed as

$$g = \left[\frac{\hbar\omega_C}{2\varepsilon_0 V_M}\right]^{1/2} \mathcal{F}(\mathbf{x}_D) \text{ where } \mathcal{F}(\mathbf{x}_D) = -\frac{\boldsymbol{\mu}^* \cdot \mathbf{E}_C(\mathbf{x}_D)}{\sqrt{\max[\varepsilon(\mathbf{x})|\mathbf{E}_C(\mathbf{x})|^2]}} \tag{33}$$

$\mathcal{F}(\mathbf{x}_D)$ is a dimensionless factor which governs the overlap between the cavity mode and the emitter—this can be increased by placing the emitter at the field maxima, and aligning its dipole with the field polarization. Clearly, decreasing the mode volume V_M increases the strength of light–matter interaction—an overview of the mode volumes achievable by typical optical cavity designs is given in Section 3.2. The full Hamiltonian for the cavity–emitter system, including the energies of the emitter and the cavity is

$$\hat{H} = \omega_C\hat{a}^\dagger\hat{a} + \omega_E\hat{\sigma}^\dagger\hat{\sigma} + \hat{H}_I \tag{34}$$

wherein we have expressed the emitter Hamiltonian (assuming the ground state to be at 0 energy) as $\omega_E|e\rangle\langle e| = \omega_E\sigma^\dagger\sigma$. As a consequence of the rotating wave approximation, this Hamiltonian conserves the total excitation number $\hat{n} = \hat{a}^\dagger\hat{a} + \hat{\sigma}^\dagger\hat{\sigma}$ for the emitter–cavity system (this can be shown by verifying that $[\hat{H}, \hat{n}] = 0$). This Hamiltonian can be exactly diagonalized and for each eigenvalue $n+1$ of $\hat{n}$, there are two eigenvectors, $|\phi_n^+\rangle$ and $|\phi_n^-\rangle$, which are entangled states of the cavity mode and the emitter known as polaritons. Their eigenfrequencies ω_n^+ and ω_n^- are given by

$$\omega_n^\pm = n\omega_C + \delta \pm \left[(n+1)|g|^2 + \delta^2\right]^{1/2} \tag{35}$$

where $2\delta = \omega_E - \omega_C$ is the detuning of the emitter frequency from the cavity frequency. These eigenfrequencies are plotted in **Figure 2**a as a function of δ. In the limit of large detuning, $|\delta| \to \infty$, the eigenfrequencies of the Jaynes–Cummings Hamiltonian tend to the eigenfrequencies that would be obtained if the cavity and emitter were uncoupled. A similar trend can be seen in the variation of the eigenstates $|\phi_n^\pm\rangle$ with δ (Figure 2b). Moreover, it can be seen from Equation (35) that when the emitter and cavity are resonant ($\delta = 0$) the eigenfrequencies of the coupled system correspond to the same eigenvalue of $\hat{n}$ split by $2g\sqrt{n+1}$. A consequence of this splitting is a coherent exchange of energy between the emitter and cavity if one of them is initially excited. For example if the emitter is initialized in its excited state and the cavity in its ground state (i.e., $|\Psi(t=0)\rangle = |e, 0\rangle$), then the state at time t can be expressed as

$$\left|\Psi(t)\right\rangle = \exp(-\mathrm{i}\omega_0 t)\left[\cos Gt|e, 0\rangle - \exp(\mathrm{i}\phi)\sin Gt|g, 1\rangle\right] \tag{36}$$

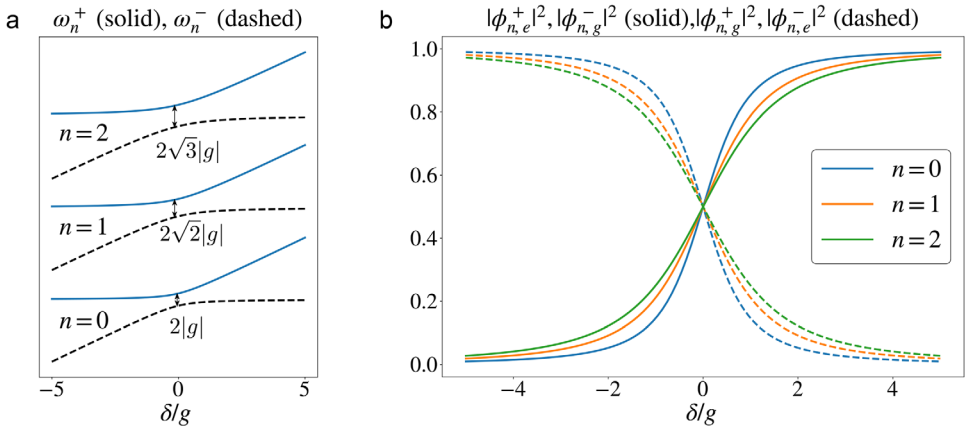

Figure 2. Eigenstructure of the Jaynes–Cummings Hamiltonian. a) The eigenfrequencies ω_n^+ and ω_n^- with the n-excitation subspace as a function of $\delta = (\omega_E - \omega_C)/2$. b) The components of the n-excitation eigenstates $|\phi_n^\pm\rangle$ as a function of δ. These components are defined as the projection of the eigenstates on the undressed cavity–emitter states: $\phi^\pm_{n,e} = \langle n, e|\phi_n^\pm\rangle$ and $\phi^\pm_{g,n} = \langle g, n+1|\phi_n^\pm\rangle$

where we have assumed that both the emitter and the cavity mode are at the same frequency $\omega_E = \omega_C = \omega_0$, and represented the coupling constant g as $G\exp(i\phi)$. It can immediately be seen from this result that the probability $P_e(t)$ of the emitter being in the excited state at time t is given by

$$P_e(t) = \cos^2 Gt \tag{37}$$

The cavity and emitter thus exchange energy periodically with the period $(2\pi/G)$ being determined by the strength of coupling in between the two systems)—this is in stark contrast to an exponential decay of the emitter energy when they couple to a continuum of modes (e.g., bulk media or waveguide—see below).

Experimentally realizable Jaynes–Cummings systems necessarily have losses in the cavity mode—these can be modeled by using the Hamiltonian of a lossy cavity given by Equation (2). The full Hamiltonian for a lossy Jaynes–Cummings Hamiltonian then becomes

$$H = \omega_C \hat{a}^\dagger \hat{a} + \omega_E \hat{\sigma}^\dagger \sigma + g\sigma a^\dagger + g^* a\sigma^\dagger + \int_{-\infty}^{\infty} \omega \hat{b}^\dagger(\omega)\hat{b}(\omega)\mathrm{d}\omega + \xi \int_{-\infty}^{\infty} \left[\hat{b}(\omega)\hat{a} + \hat{a}\hat{b}^\dagger(\omega)\right]\mathrm{d}\omega \tag{38}$$

In this Hamiltonian, there are two-relevant parameters that govern the dynamics of the system—the cavity–emitter coupling constant g and the cavity–bath coupling constant ξ. Further insight into the behavior of this system can be gained if we were to consider the time evolution of an initially excited emitter—that is, $|\Psi(0)\rangle = |e, 0, \mathrm{vac}\rangle$. At time t, the excitation can be either in the two-level system, in the cavity mode or in the bath modes:

$$|\Psi(t)\rangle = A_e(t)|e, 0, \mathrm{vac}\rangle + A_c(t)|g, 1, \mathrm{vac}\rangle + \int_{-\infty}^{\infty} A_g(t;\omega)\hat{b}^\dagger(\omega)|\mathrm{g}, 0, \mathrm{vac}\rangle\mathrm{d}\omega \tag{39}$$

where $A_e(0) = 1, A_c(0) = 0$, and $A_g(0;\omega) = 0$. With these initial conditions, the Schrodinger's equation can be readily integrated to obtain explicit expressions for $A_e(t)$, $A_g(t;\omega)$, and $A_c(t)$ as a function of t. In the following analysis, we assume that the cavity and the emitter are resonant with each other (i.e., $\omega_E = \omega_C = \omega_0$). In the *strong coupling regime*, where the cavity coupling strength dominates over the decay rate of the cavity, that is, $g > \kappa/4$ (where $\kappa = 2\pi\xi^2$ is the decay rate of the cavity mode),

$$P_e(t) = |A_e(t)|^2 = \exp\left(-\frac{\kappa t}{2}\right)\left|\cos\Gamma t + \frac{\kappa}{4\Gamma}\sin\Gamma t\right|^2 \tag{40}$$

where $\Gamma = \sqrt{G^2 - \kappa^2/16}$. In this regime, the emitter and cavity also periodically exchange energy between each other—however, this exchange of energy is damped due to the losses in the cavity. In the *weak coupling regime*, where $g < \kappa/4$, the probability of the emitter being in the excited state is given by

$$P_e(t) = |A_e(t)|^2 = \exp\left(-\frac{\kappa t}{2}\right)\left|\cosh\Gamma t + \frac{\kappa}{4\Gamma}\sinh\Gamma t\right|^2 \tag{41}$$

where $\Gamma = \sqrt{\kappa^2/16 - G^2}$. Here, the emitter and the cavity no longer periodically exchange energy with each other—the dynamics of the emitter resembles an exponential decay. More specifically, as $t \to \infty$, $P_e(t) \approx \exp(-(\kappa/2 - 2\Gamma)t)$, which allows the extraction of an effective emitter decay rate γ_{eff} given by

$$\gamma_{\mathrm{eff}} = \frac{\kappa}{2} - 2\Gamma \approx \frac{4G^2}{\kappa} \tag{42}$$

Within the weak coupling regime, the effective decay rate of the emitter can be modified by controlling the quality factor (or the decay rate) of the optical cavity—in particular, a high quality factor cavity would increase γ_{eff}, thus speeding up the emitter decay. This enhancement of the decay rate is referred to as Purcell enhancement. To summarize, the strong coupling regime is characterized by the emitter emitting into the cavity mode followed by reabsorbing the emitted energy, while it irreversibly decays into the lossy cavity mode in the weak coupling regime.

2.4.2. Emitters Coupling to Waveguides

Within the rotating-wave and Markov approximation, using Equation (7), we obtain the following interaction Hamiltonian for the emitter–waveguide system:

$$\hat{H}_I = \int_{\omega_c}^{\infty} \left[g(\omega)\hat{\sigma}\hat{a}^{\dagger}(\omega) + g^{*}(\omega)\hat{a}(\omega)\hat{\sigma}^{\dagger} \right] \mathrm{d}\omega \tag{43}$$

Here $g(\omega)$, the coupling strength between the emitter and the waveguide mode at frequency ω, is given by

$$g(\omega) = -\left[\frac{\hbar\omega_E}{2\varepsilon_0 v_G(\omega) \int_{\Gamma} \varepsilon(\boldsymbol{\rho}) |E(\boldsymbol{\rho}; \beta(\omega))|^2 \mathrm{d}^2\boldsymbol{\rho}} \right]^{1/2} \boldsymbol{\mu}^{*} \cdot \mathbf{E}(\boldsymbol{\rho}_E; \beta(\omega)) \tag{44}$$

where we have assumed that the emitter is located at $x = 0$ with a transverse coordinate $\boldsymbol{\rho}_E$. In most quantum optical systems, the spread in frequencies ω with which the emitter interacts is much smaller than the frequency-scale over which $g(\omega)$ varies—consequently, it is reasonable to approximate $g(\omega)$ with $g(\omega_E)$ in Equation (43). Further, when the frequency of the emitter is far detuned from the cut-off frequency ω_c of the waveguide, it is reasonable to extend the lower limit of the integral in Equation (43) to $-\infty$. With these two approximations, collectively called the Markovian approximation,[49] we obtain the following expression for the interaction Hamiltonian:

$$\hat{H}_I \approx \int_{-\infty}^{\infty} \left[g(\omega_E)\hat{\sigma}\hat{a}^{\dagger}(\omega) + g^{*}(\omega_E)\hat{a}(\omega)\hat{\sigma}^{\dagger} \right] \mathrm{d}\omega \tag{45}$$

The Markovian approximation can alternatively be stated as treating the waveguide to be an infinite-bandwidth system—that is, all the frequencies in the waveguide mode interact equally with the emitter. The coupling constant $g(\omega_E)$ that governs the strength of the emitter–waveguide interaction within the Markovian approximation can be expressed as

$$\begin{aligned} g(\omega_E) &= -\left[\frac{\hbar\omega_E}{2\varepsilon_0 S_M v_G(\omega_E)} \right]^{1/2} \mathcal{F}(\boldsymbol{\rho}_E) \text{ where } \mathcal{F}(\boldsymbol{\rho}_E) \\ &= -\frac{\mu^{*} \cdot \mathbf{E}(\boldsymbol{\rho}_E; \beta(\omega_E))}{\sqrt{\max[\varepsilon(\boldsymbol{\rho}) |E(\boldsymbol{\rho}; \beta(\omega_E))|^2]}} \end{aligned} \tag{46}$$

where $\mathcal{F}(\boldsymbol{\rho}_E)$ is a measure of the overlap of the emitter's dipole with the waveguide mode, and S_M is the mode area:

$$S_M = \frac{\int_{\Gamma} \varepsilon(\boldsymbol{\rho}) |\mathbf{E}(\boldsymbol{\rho}; \beta(\omega_E))|^2 \mathrm{d}^2\boldsymbol{\rho}}{\max[\varepsilon(\boldsymbol{\rho}) |\mathbf{E}(\boldsymbol{\rho}; \beta(\omega_E))|^2]} \tag{47}$$

Similar to cavities, the coupling between waveguides and emitters can be made stronger by reducing the mode area S_M or by increasing the spatial or polarization overlap between the emitter dipole and the waveguide mode. The full Hamiltonian for the waveguide–emitter system can be expressed as

$$H = \omega_E \hat{\sigma}^{\dagger}\hat{\sigma} + \int_{-\infty}^{\infty} \omega \hat{a}^{\dagger}(\omega)\hat{a}(\omega)\mathrm{d}\omega + \int_{-\infty}^{\infty} [g\hat{\sigma}\hat{a}^{\dagger}(\omega) + g^{*}\hat{a}(\omega)\hat{\sigma}^{\dagger}]\mathrm{d}\omega \tag{48}$$

The behavior of this system has some marked differences from that of a cavity–emitter system. One of the most fundamental difference is that excitations in emitters coupled to waveguides exponentially decay into the waveguide mode, as opposed to periodically exchanging energy with it. In particular, if the emitter is initially in an excited state and the waveguide in vacuum state, $|\Psi(0)\rangle = |e\rangle|\mathrm{vac}\rangle$, then at time t, the state of the waveguide–emitter system is given by

$$|\Psi(t)\rangle = A_e(t)|e\rangle|\mathrm{vac}\rangle + \int_{-\infty}^{\infty} A_g(t;\omega)\hat{a}^{\dagger}(\omega)|\mathrm{vac}\rangle\mathrm{d}\omega \tag{49}$$

where

$$A_e(t) = \exp\left(-\frac{\gamma t}{2}\right)\exp(-\mathrm{i}\omega_E t) \tag{50}$$

$$A_g(t;\omega) = \frac{g(\omega_E)\left[\exp\{-(\mathrm{i}\omega_E + \gamma/2)t\} - \exp(-\mathrm{i}\omega t)\right]}{\omega - \omega_E + \mathrm{i}\gamma/2} \tag{51}$$

where $\gamma = 2\pi|g(\omega_E)|^2$. This process is the spontaneous emission of the emitter into the waveguide mode and γ is the spontaneous emission decay rate. Using Equation (46), γ can be explicitly expressed in terms of the guided mode's parameters:

$$\gamma = \frac{\pi\hbar\omega_E |\mathcal{F}(\omega_E)|^2}{\varepsilon_0 S_M v_G(\omega_E)} \tag{52}$$

This expression shows that the spontaneous emission rate γ can be engineered by controlling the group velocity $v_G(\omega_E)$ as well as the mode area S_M of the waveguide. Equation (52) indicates that a possible route to enhance the Purcell effect in waveguide structures is the use of slow light—this approach is complementary to using a high quality factor cavity within the weak-coupling regime to enhance emission from the emitters.

Finally, waveguides (or more generally, loss channels) can be used to drive emitters coherently—this corresponds to initializing the loss channel into a coherent state: $|\Psi(0)\rangle = |\Psi_E\rangle|\alpha(\omega)\rangle$, where $|\alpha(\omega)\rangle$ is a coherent state as defined in Equation (26) and $|\Psi_E\rangle$ is the state of the emitter. This is a suitable model for theoretically analyzing the response of an emitter on exciting it with a laser. A closer correspondence to the semiclassical description of light–matter interaction can be established by describing the system in terms of a state $|\tilde{\Psi}(t)\rangle$ which is related to the true state $|\Psi(t)\rangle$ by a unitary transformation on $|\Psi(t)\rangle$:

$$\begin{aligned} \left|\tilde{\Psi}(t)\right\rangle = \exp\left(\int \left[\alpha^{*}(\omega)\hat{a}(\omega)\exp(-\mathrm{i}\omega t) - \hat{\alpha}(\omega)\hat{a}^{\dagger}(\omega)\exp(\mathrm{i}\omega t) \right] \mathrm{d}\omega \right) \\ \times \left|\Psi(t)\right\rangle \end{aligned} \tag{53}$$

then the initial condition translates to $|\tilde{\Psi}(0)\rangle = |\Psi_E\rangle|\mathrm{vac}\rangle$ equivalent Hamiltonian $\tilde{H}(t)$ governing the evolution of the state $|\tilde{\Psi}(t)\rangle$ is given by (refer to Appendix C of ref. [30]):

$$\tilde{H}(t) = \hat{H} + [\Omega^{*}(t)\hat{\sigma} + \Omega(t)\hat{\sigma}^{\dagger}] \tag{54}$$

where $\Omega(t)$ is the "driving pulse" given by

$$\Omega(t) = g^*(\omega_E)\int_{-\infty}^{\infty}\alpha(\omega)\exp(-i\omega t)\mathrm{d}\omega \tag{55}$$

This driving term is similar to that obtained in a treatment of light–matter interaction in which the optical fields are treated classically. Addition of this driving term to the Hamiltonian allows us to solve a problem in which the loss channel is initially in the vacuum state—such a problem can be numerically analyzed within the master-equation framework[50] or the scattering matrix framework.[30,51,52]

2.5. Two-Time Second-Order Correlation Function for Characterizing Single-Photon Sources

A very popular experimental metric[50,53] for characterizing states emitted from single-photon sources is the two-time second-order correlation function $g^{(2)}(t_1, t_2)$, which is a measure of the joint probability of detecting a photon at both the time instants t_1 and t_2. Mathematically, assuming that the detector is located at $x = L$, this is defined by (note that all the operators are the position annihilation operators):

$$g^{(2)}(t_1,t_2) = \frac{\langle\Psi|\hat{a}^\dagger(t_1;L)\hat{a}^\dagger(t_2;L)\hat{a}(t_2;L)\hat{a}(t_1;L)|\Psi\rangle}{\langle\Psi|\hat{a}^\dagger(t_1;L)\hat{a}(t_1;L)|\Psi\rangle\langle\Psi|\hat{a}^\dagger(t_2;L)\hat{a}(t_2;L)|\Psi\rangle}$$
$$= \frac{\langle\Psi|\hat{a}^\dagger(L-v_Gt_1)\hat{a}^\dagger(L-v_Gt_2)\hat{a}(L-v_Gt_2)\hat{a}(L-v_Gt_1)|\Psi\rangle}{\langle\Psi|\hat{a}^\dagger(L-v_Gt_1)\hat{a}(L-v_Gt_1)|\Psi\rangle\langle\Psi|\hat{a}^\dagger(L-v_Gt_2)\hat{a}(L-v_Gt_2)|\Psi\rangle} \tag{56}$$

where $\hat{a}(t;L) = \hat{a}(L - v_G t)$ is the position annihilation operator at the location of the detector in the Heisenberg picture at time t. In a realistic experimental setting, however, the photodetector usually has a response time which is much larger than the temporal width of the light being emitted from the light source. This practical limitation prohibits the exact measurement of $g^{(2)}(t_1, t_2)$ as a function of (t_1, t_2), rather it allows the measurement of the integrated two-time correlation $g^{(2)}[0]$:[50]

$$g^{(2)}[0] = \frac{\iint\langle\Psi|\hat{a}^\dagger(t_1;L)\hat{a}^\dagger(t_2;L)\hat{a}(t_2;L)\hat{a}(t_1;L)|\Psi\rangle\mathrm{d}t_1\mathrm{d}t_2}{[\int\langle\Psi|\hat{a}^\dagger(t;L)\hat{a}(t;L)|\Psi\rangle\mathrm{d}t]^2} \tag{57}$$

Even if a precise measurement of $g^{(2)}(t_1, t_2)$ as a function of t_1 and t_2 was possible, $g^{(2)}[0]$ provides information about the two-photon statistics of the entire photon pulse. Both $g^{(2)}(t_1, t_2)$ and $g^{(2)}[0]$ have remarkably different values for different states of light, making it a suitable tool for characterizing the state of light emitted by a light source. In particular,

1. For the light emitted by an ideal single-photon source (Equation (15)), $g^{(2)}(t_1, t_2) = 0$ and $g^{(2)}[0] = 0$—a small value of $g^{(2)}[0]$ is often treated is an experimental signature of a single-photon state.
2. For light emitted from an ideal coherent source (Equation (26)), $g^{(2)}(t_1, t_2) = 1$ and $g^{(2)}[0] = 1$.
3. For a two-photon state (Equation (11) with $N = 2$),

$$g^{(2)}(t_1,t_2) = \frac{|\psi^{(2)}(x_1 = L - v_Gt_1, x_2 = L - v_Gt_2)|^2}{2\int|\psi^{(2)}(x_1 = L - v_Gt_1, x_2)|^2\mathrm{d}x_2\int|\psi^{(2)}(x_1, x_2 = L - v_Gt_2)|^2\mathrm{d}x_1} \leq \frac{1}{2} \tag{58}$$

and $g^{(2)}[0] = 1/2$.

Similarly, it is possible to define the two time first order correlation function, $g^{(1)}(t_1, t_2)$, via

$$g^{(1)}(t_1,t_2) = \frac{\langle\Psi|\hat{a}^\dagger(t_1;L)\hat{a}(t_2;L)|\Psi\rangle}{\sqrt{\langle\Psi|\hat{a}^\dagger(t_1;L)\hat{a}(t_1;L)|\Psi\rangle\langle\Psi|\hat{a}^\dagger(t_2;L)\hat{a}(t_2;L)|\Psi\rangle}} \tag{59}$$

and its integrated version, also referred to as the visibility v:

$$v = g^{(1)}[0] = \frac{\iint\langle\Psi|\hat{a}^\dagger(t_1;L)\hat{a}(t_2;L)|\Psi\rangle\mathrm{d}t_1\mathrm{d}t_2}{\int\langle\Psi|\hat{a}^\dagger(t;L)(t)\hat{a}(t;L)|\Psi\rangle\mathrm{d}t} \tag{60}$$

The visibility v is correlated with how pure the single-photon state is, and can be experimentally accessed using a Hong–Ou–Mandel interferometer (see below). It can be noted that the first order correlation function $g^{(1)}(t_1, t_2)$ is a complex number, and thus carries information of the phase relationship between the light incident on the detector at $t = t_1$ and $t = t_2$.

An experimental difficulty in the measurement of the two-time second-order correlation function is that most photodetectors have a dead time—this refers to the time after a photodetection for which the detector is no longer able to register incoming photons. This dead time is often larger than the pulsewidth of the light emitted by the photon source, thereby making it impossible to measure the two-time correlation with just one detector. An alternative scheme to get around this issue is the Hanbury–Brown and Twiss interferometer (HBT)—this scheme (**Figure 3**a) splits the light emitted by the source into two waveguides via a 50–50 beam splitter ($\theta = \pi/4$), and then performs photodetection in the two waveguides separately.[50] The phase shift φ shown in the setup models random variation in the path lengths of the two arms of the interferometer due to environmental fluctations—the result of an experimental measurement performed over repeated trial effectively averages over this phase shift. The two-time correlation function measured by this setup is then given by

$$g^{(2)}_{\mathrm{HBT}}(t_1,t_2) \approx \frac{\mathbb{E}_\varphi[\langle\Psi|\hat{a}^\dagger(t_1;L)\hat{b}^\dagger(t_2;L)\hat{b}(t_2;L)\hat{a}(t_1;L)|\Psi\rangle]}{\mathbb{E}_\varphi[\langle\Psi|\hat{a}^\dagger(t_1;L)\hat{a}(t_1;L)|\Psi\rangle]\mathbb{E}_\varphi[\langle\Psi|\hat{b}^\dagger(t_2;L)\hat{b}(t_2;L)|\Psi\rangle]} \tag{61}$$

and its integrated version:

$$g^{(2)}_{\mathrm{HBT}}[0] \approx \frac{\iint\mathbb{E}_\varphi[\langle\Psi|\hat{a}^\dagger(t_1;L)\hat{b}^\dagger(t_2;L)\hat{b}^\dagger(t_2;L)\hat{a}^\dagger(t_1;L)|\Psi\rangle\mathrm{d}t_1\mathrm{d}t_2]}{\int\mathbb{E}_\varphi[\langle\Psi|\hat{a}^\dagger(t;L)\hat{a}(t;L)|\Psi\rangle\mathrm{d}t]\int\mathbb{E}_\varphi[\langle\Psi|\hat{b}^\dagger(t;L)\hat{b}(t;L)|\Psi\rangle\mathrm{d}t]} \tag{62}$$

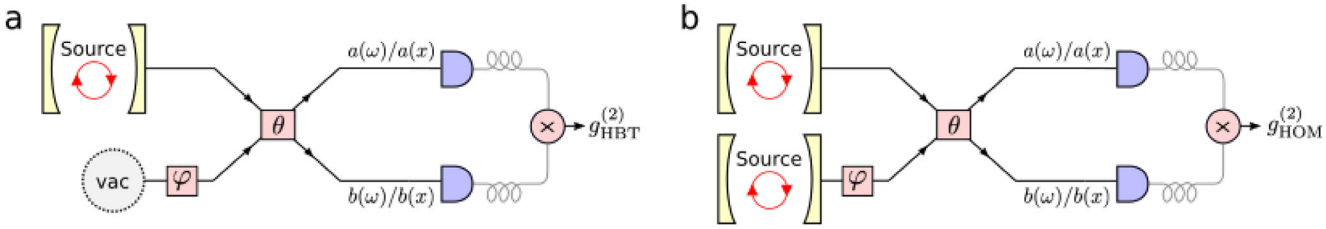

Figure 3. Interferometers for characterizing light sources. Schematic of a) Hanbury–Brown–Twiss interferometer and b) Hong–Ou–Mandel interferometer. In both cases, the beam splitter is assumed to be a 50–50 beam splitter ($\theta = \pi/4$) and the phase shift ϕ models random variations between the path lengths of the two branches of the interferometer. Adapted under the terms of the Creative Commons Attribution 3.0 license.[50] Copyright 2016, The Authors, Published by IOP Publishing Ltd on behalf of Deutsche Physikalische Gesellschaft.

Here, $\mathbb{E}_{\varphi}[\cdot]$ indicates an average over the phase φ between the two arms of the interferometer. We note that this averaging has no impact on the measured two-time correlation function in the Hanbury–Brown and Twiss interferometer since one of the arms of the interferometers is in the vacuum state, but has an impact on the two-time correlation function measured in the Hong–Ou–Mandel interferometer (described below) since both the arms of the interferometer are excited. As is shown in the Appendix B, this is identical to the two-time correlation function defined in Equation (56).

For single-photon states, another important performance metric is the indistinguishability of the single-photon sources—the fidelity of any information processing or computing scheme that relies on the ability to entangle the light emitted by two single-photon sources would ultimately be limited by how distinguishable the single-photon sources are. Experimentally, the indistinguishability of two single-photon sources can be determined by the Hong–Ou–Mandel interferometer (HOM)—this scheme (Figure 3b) combines the two single-photons at a beam splitter and performs photodetection at the two waveguides separately.[50] We define the integrated two-time correlation for this interferometer $g^{(2)}_{\mathrm{HOM}}[0]$ via

$$g^{(2)}_{\mathrm{HOM}}[0] \approx \frac{\iint \mathbb{E}_{\varphi}[\langle\Psi|\hat{a}(t_1;L)\hat{b}(t_2;L)\hat{b}^{\dagger}(t_2;L)\hat{a}^{\dagger}(t_1;L)|\Psi\rangle]\mathrm{d}t_1\mathrm{d}t_2}{\int \mathbb{E}_{\varphi}[\langle\Psi|\hat{a}^{\dagger}(t;L)\hat{a}(t;L)|\Psi\rangle]\mathrm{d}t \int \mathbb{E}_{\varphi}[\langle\Psi|\hat{b}^{\dagger}(t;L)\hat{b}(t;L)|\Psi\rangle]\mathrm{d}t} \tag{63}$$

In case both the sources are assumed to be identical, using Equations (B18) and (B20), $g^{(2)}_{\mathrm{HOM}}[0]$ can be expressed in terms of the visibility v (Equation (60)) and the integrated second-order two-time correlation $g^{(2)}[0]$ of the source:

$$g^{(2)}_{\mathrm{HOM}}[0] = \frac{g^{(2)}[0]}{2} + \frac{1-v}{2} \tag{64}$$

This decomposes $g^{(2)}_{\mathrm{HOM}}[0]$ into two contributing factors—visibility v related to the purity of the emitted single-photon state and $g^{(2)}[0]$ indicating the significance of the multiphoton contributions to the emitted state.[54] For example, as is shown in the Appendix B, for a Hong–Ou–Mandel interference between two single-photon sources, this correlation function can be expressed in terms of the density matrices of the two sources:

$$g^{(2)}_{\mathrm{HOM}}[0] = \frac{2P_{1,a}P_{2,a}}{(P_{1,a}+P_{2,a})^2} \times \left[1 - \int_{-\infty}^{\infty}\int_{-\infty}^{\infty} \rho^{(1)*}_{a}(\omega_1,\omega_2)\rho^{(1)}_{b}(\omega_1,\omega_2)\mathrm{d}\omega_1\mathrm{d}\omega_2\right] \tag{65}$$

where the subscripts a and b refer to whether the sources emit into the waveguide labeled as a or b, and $P_1, \rho^{(1)}(\omega_1,\omega_2)$ have been defined in Equation (16). Measurement of $g^{(2)}_{\mathrm{HOM}}[0]$ provides information about the purity and indistinguishability of the two photons. To see this, it is useful to specialize this expression for two limiting cases:

1. *Both Sources Emitting Pure States*: In this case, $\rho^{(1)}(\omega_1,\omega_2) = \psi^{(1)*}(\omega_1)\psi^{(1)}(\omega_2)$ (where $\psi^{(1)}(\omega)$ is defined in Equation (15)), and $g^{(2)}_{\mathrm{HOM}}[0]$ reduces to

$$g^{(2)}_{\mathrm{HOM}}[0] = \frac{2P_{1,a}P_{1,b}}{(P_{1,a}+P_{1,b})^2}\left[1 - \left|\int_{-\infty}^{\infty}\psi^{(1)*}_{a}(\omega)\psi^{(1)}_{b}(\omega)\mathrm{d}\omega\right|^2\right] \tag{66}$$

   from which it can clearly be seen that $g^{(2)}_{\mathrm{HOM}}[0] = 0$ indicates that the two sources have identical complex spectra. $g^{(2)}_{\mathrm{HOM}}[0]$ thus provides information about how distinguishable two single photon sources are.
2. *Both Sources Being Identical*: In the case where both sources are identical and emit single photons with unity probability, but not necessarily in a pure state, $g^{(2)}_{\mathrm{HOM}}[0]$ simplifies to

$$g^{(2)}_{\mathrm{HOM}}[0] = \frac{1}{2}\left[1 - \int_{-\infty}^{\infty}\int_{-\infty}^{\infty}|\rho^{(1)}(\omega_1,\omega_2)|^2\mathrm{d}\omega_1\mathrm{d}\omega_2\right] = \frac{1}{2}\left[1 - \mathrm{Tr}(\hat{\rho}^2)\right] \tag{67}$$

   and the visibility $v = \mathrm{Tr}(\hat{\rho}^2)$. In this case, it can be seen that $g^{(2)}_{\mathrm{HOM}}[0]$ (or visibility) provides direct information about the trace purity of the single-photon sources—a pure state has $g^{(2)}_{\mathrm{HOM}}[0] = 0$. While the trace purity is not in general accessible from a Hong–Ou–Mandel experiment when there are multiphoton components of emission present for the sources, recent work has shown how to access the trace purity using methods beyond the scope of this Review.[54]

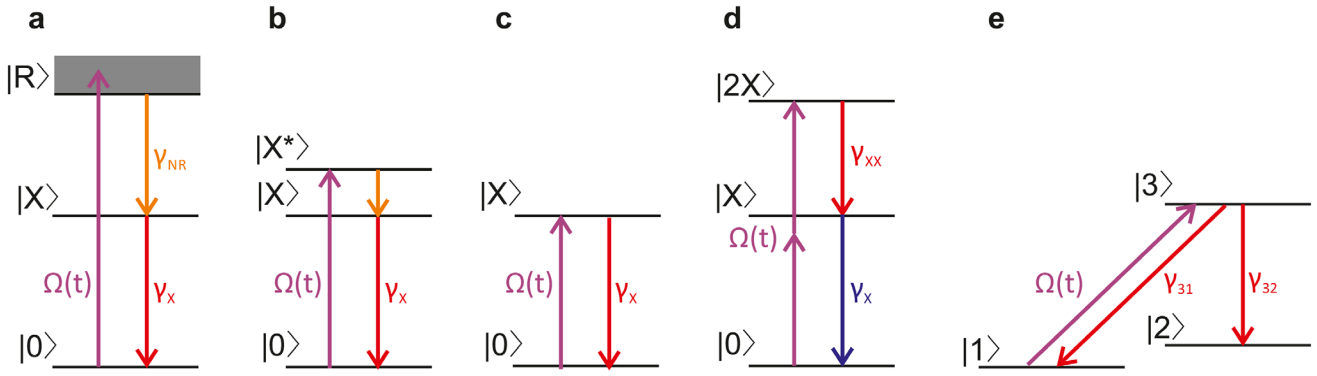

Figure 4. Schemes for non-classical light generation. a) Non-resonant excitation above bandgap or in the wetting layer. b) Quasi-resonant excitation via an excited state (p-shell). c) Resonant excitation. d) Two-photon excitation of $|2X\rangle$. e) Lambda scheme.

3. Single Photons

3.1. Schemes for Single Photon Generation

The type of non-classical light that is most commonly generated using quantum dots are single photons. They are the key ingredient for many quantum technologies, such as single-photon based quantum key distribution,[1] linear optical quantum computing,[3,8] and boson sampling.[9,55,56] While for applications such as quantum key distribution using the BB84 protocol only a decent single-photon purity is required, applications such as linear optical quantum computing and boson sampling that are based on interference of single photons require a very high single-photon purity and indistinguishability. Moreover, single photons with high purity and indistinguishability can be used to create more complex quantum states of light.[57,58]

To generate single photons from QDs, multiple schemes with different advantages and disadvantages have been established over the years. These schemes are summarized in **Figure 4**.

In the non-resonant excitation scheme (Figure 4a) a short laser pulse creates electrons and holes either above the bandgap or in the wetting layer of the QD.[59,60] These charge carriers relax into the lowest energy states of the QD via phonon-mediated processes where they recombine radiatively. If the QD is filled with multiple charge carriers, due to the Coulomb interaction, each charge configuration emits at a different frequency and per excitation pulse only one photon is expected to be emitted at the energy of the neutral exciton X. This is the most simple method for generating single photons from QDs since the energy of the excitation laser does not have to be controlled precisely. Moreover, since the energy between excitation and emission is significantly different, the signal can easily be separated from the excitation laser by frequency filtering. In this scheme, the purity is limited by charge carriers that stay long enough in the wetting layer/above bandgap to allow for a refilling of the QD and emission of a second photon after a first photon has been emitted.[61] Also, the degree of indistinguishability that can be achieved is limited due to the excitation timing jitter from the incoherent relaxation.[50]

To suppress re-excitation, the QD can also be excited quasi-resonantly via its p-shell (Figure 4b). This has been shown to improve the purity.[36] However, the indistinguishability is still limited by the excitation timing jitter from the incoherent relaxation and although the single-photon purity is better than in scheme (a), it is still not perfect since if the relaxation and emission of a photon occur already during the presence of the excitation laser pulse the system can be re-excited and emit a second photon.[50] Depending on the ratio of the rate of the incoherent relaxation and the photon emission the limit of $g^{(2)}[0]$ will be between those of schemes (c) and (d) discussed below.

To completely eliminate excitation timing jitter resonant excitation can be performed (Figure 4c).[62] Since the excitation laser and signal have the same energy here the excitation laser needs to be filtered out either by using cross-polarized detection or by using different spatial modes. This scheme has been widely used over the past years[62–68] and regularly demonstrated $g^{(2)}[0] < 0.01$ and high indistinguishability with $\nu > 0.97$ without Purcell enhancement of the emission rate[62] and visibility $\nu > 0.99$ with Purcell enhancement[65] (see Section 3.2). The finite values of the $g^{(2)}[0]$ and $1-\nu$ result from re-excitation.[47,50] If a photon is already emitted during the presence of the excitation laser pulse there is a finite probability that the two-level system is re-excited and emits a second photon.[29,69] The value of $g^{(2)}[0]$ for a resonantly driven two-level system is presented in **Figure 5**a as a function of the pulse length (normalized to the excited state lifetime) for exciting with π-pulses of Gaussian shape. For short pulses, $g^{(2)}[0]$ increase linearly with the pulse length and saturates at 1 for long pulses. The value of $g^{(2)}_{\mathrm{HOM}}[0]$ for a resonantly driven two-level system is presented in Figure 5b as a function of the pulse length (normalized to the excited state lifetime) for exciting with π-pulses of Gaussian shape. It is decomposed into $g^{(2)}[0]/2$ and $(1-\nu)/2$ and also increases linearly for short pulses.

Recently, another scheme was used to demonstrate very pure single photon generation with values $g^{(2)}[0] \approx 10^{-5}$.[32,70] In this scheme (Figure 4d), a two-photon excitation process coherently prepares the system in the $2X$ state.[71–73] Since due to the Coulomb interaction the energy of $2X$ is lower than twice the X energy the energy of the excitation laser is detuned from the $2X$ as well as the X transition. Single photons can then be obtained by frequency filtering either on the X or $2X$ transition. Since re-excitation is only possible after the radiative cascade has returned the system to the ground state it is largely suppressed.[32,70] The dependence of $g^{(2)}[0]$ on the pulse length is presented in Figure 5c

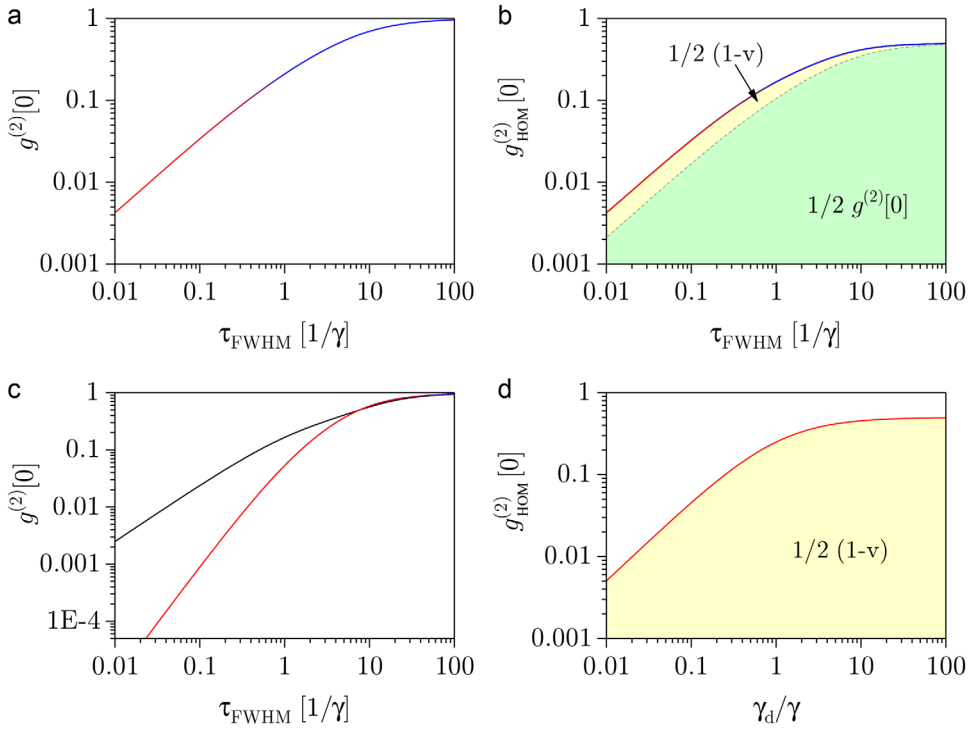

Figure 5. Dynamics of single-photon generation. a) $g^{(2)}[0]$ as a function of the pulse length for a resonantly driven two-level system. b) $g^{(2)}_{HOM}[0]$ as a function of the pulse length for a resonantly driven two-level system. c) $g^{(2)}[0]$ as a function of the pulse length for a resonantly driven two-level system (black) and two-photon excitation of a three-level system (red). d) $g^{(2)}_{HOM}[0]$ for a lambda system as a function of the dephasing rate. (a,b) Adapted from ref. [50], (c) adapted from ref. [32] under the terms of a Creative Commons Attribution license. Copyright 2016, 2018, The Author(s); Published by IOP Publishing Ltd on behalf of Deutsche Physikalische Gesellschaft, and Springer Nature, respectively.

for a resonantly driven two-level system (black) and two-photon excitation of a three-level system (red) for exciting with square pulses. The two-photon excitation of a three-level system shows significantly lower values than the resonantly excited two-level system. Here, we used $\gamma_{2X} = 2\gamma_X$. Specifically, for short pulses $g^{(2)}[0]$ scales with $(\gamma\tau)^2$ which results for short pulses in an improvement of $g^{(2)}[0]$ as large as several orders of magnitude compared to a resonantly excited two-level system.

Another scheme that was recently demonstrated with QDs consists of a lambda system with two ground states ($|1\rangle$ and $|2\rangle$) and one excited state ($|3\rangle$) whereby the decay rate γ_{32} is much larger than γ_{31} (Figure 4e).[74–77] After the system is initialized in the state $|1\rangle$ a laser pulse drives the system into state $|3\rangle$ from where it decays to state $|2\rangle$ emitting a photon. Such a system can be realized by a singly charged QD in a Faraday geometry magnetic field (B field parallel to the growth direction) where the transition 3-1 should not be optically active but in fact weakly couples to light while the transition 3-2 couples to circularly polarized light.[77] Alternatively, a singly charged QD in a Voigt geometry magnetic field (B field perpendicular to the growth direction) can be used. Here, the energy levels consists of a double lambda system where the vertical transitions couple to vertically polarized light while the diagonal transitions couple to horizontally polarized light. Using a vertically polarized cavity mode which is slightly detuned from the QDs transition results in the scenario depicted in Figure 4e.[74–76] In this case the single photons are Raman photons which are emitted into the cavity mode without populating the excited state of the QD. Since in this scheme the initial state and final state are different re-excitation should be entirely suppressed leading to $g^{(2)}[0] = 0$ as long as the spin relaxation rate is much longer than the pulse length. Therefore, also the indistinguishability is only limited by the spin-dephasing of the ground states as well as coupling to acoustic phonons. The dependence of $g^{(2)}_{HOM}[0]$ on the dephasing rate is presented in Figure 5d. A major advantage of this scheme is that it allows to create single photons where the waveform can be arbitrarily controlled by the temporal shape of the excitation laser pulse.[75–77] The disadvantage of this scheme is that it is difficult to implement and that the rate of single-photon generation will be limited by the time that it takes to re-pump the system into state $|1\rangle$.

In addition to the inherent limitations of ideal few-level systems discussed so far QDs are subject to limitations that result from experimental constraints or the semiconductor environment. For example cross-polarized techniques that filter out the excitation laser also reduce the brightness of the signal. On the other hand, coupling to acoustic phonons in the environment[78–81] damps Rabi oscillations which reduces the probability of exciting the systems[82,83] and, thus also reduces the brightness. Since coupling to acoustic phonons depends on the amplitude of the driving laser, this effect is more pronounced for shorter pulses. For example, exciting with a π-pulse of a few ps length typically results in an excitation probability around 80-90%.[73] In addition, fluctuations in the electronic environment lead to spectral diffusion of the emission frequency which further

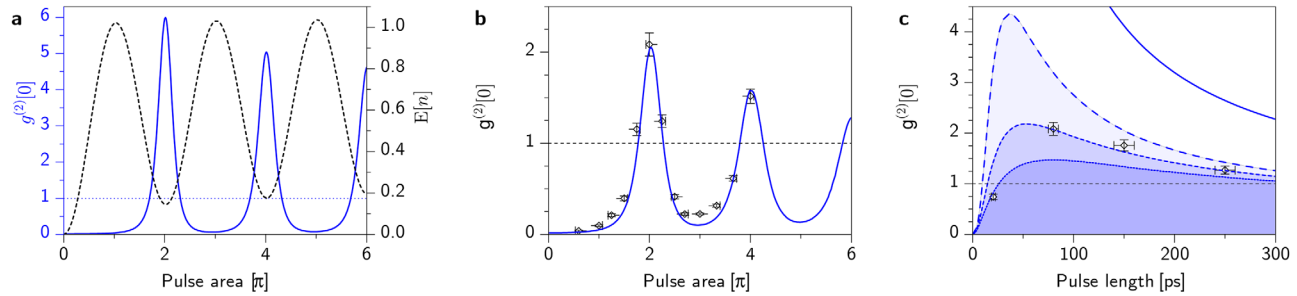

Figure 6. Generation of two-photon pulses from a resonantly driven two-level system. a) Theoretical $g^{(2)}[0]$ (blue solid) and expected photon number (black dashed) versus pulse area for an ideal two-level system. Oscillations between antibunching (at odd π-pulses) and bunching (at even π-pulses) are observed. b) Experimentally measured $g^{(2)}[0]$ versus pulse area confirming the prediction from (a). Blue curve represents quantum simulations using the experimentally measured lifetime, pulse length, phonon coupling, and chirp of the laser pulses. Dashed black line represents statistics of the incident laser pulse. c) Experimental second-order coherence measurements $g^{(2)}[0]$ versus pulse length (using 2π-pulses for excitation). Solid blue line represents emission from an ideal two-level quantum system, long dashed blue line represents inclusion of dephasing, short dashed blue line represents addition of a 2.7% chirp in bandwidth, and short dotted blue line represents addition of a further 2.7% chirp in bandwidth. Adapted with permission.[29] Copyright 2017, Springer Nature.

limits the obtainable indistinguishability. This effect is less pronounced in resonant excitation schemes which avoid the creation of free charge carriers. In general, a higher indistinguishability is observed for QDs embedded in diode structures which, as discussed above show less spectral diffusion due to the stabilization of the electronic environment.

In the discussion of the generation of single photons from a resonantly driven two-level system above, we have considered only excitation pulses with a pulse area of π. However, it was recently shown that also the pulse area has a strong impact on the emitted quantum light and that a resonantly driven two-level system can even predominantly emit two-photon pulses.[29] For an ideal two-level system the expected number of emitted photons and $g^{(2)}[0]$ are presented in **Figure 6**a as a function of the pulse area for pulses of length $\tau = 1/(10\gamma)$. Oscillations are observed in $g^{(2)}[0]$ which are out of phase with the Rabi oscillations and which can be understood as follows. For exciting with pulse areas of odd multiples of π the emission consist mainly of single photons whereby the non-zero value of $g^{(2)}[0]$ results from the emission of a photon and re-excitation during the presence of the laser pulse as discussed above. For even multiples of π, the emission consists mainly of the vacuum state since the Rabi oscillation returns the system to the ground state. However, if emission occurs it is most likely to occur when the system is in its excited state—exactly after an area of π has been absorbed. Then, the remaining area of the pulse is also π, that is, the system is re-excited and emits a second photon with very high probability which results in the observed bunching of $g^{(2)}[0]$. An experimental measurement for exciting a two-level system with a lifetime of 602ps (formed by a charged QD) with 80 ps long pulses is presented in Figure 6b and clearly confirms the theoretical prediction. Here, the blue line is a fit which takes into account the measured lifetime, measured pulse length and measured non-idealities (phonon coupling, chirp of the laser pulse). The dependence of the bunching on the pulse length for exciting with 2π pulses is presented in Figure 6c. When taking into account the measured deviations from an ideal two-level system (different lines), a good agreement between theory and experiment is observed, further confirming that a resonantly driven two-level system can preferentially emit pulses where the single-photon probability is below the two-photon probability.

3.2. Resonators (Weak Coupling Regime)

Resonators are commonly used to redistribute the emission such that it can be efficiently collected. In this section, we discuss the QDs coupled to resonators in the weak coupling regime which is primarily used for an efficient extraction of the photons for off-chip applications.

Resonators with small mode volume and high quality factors (Q-factors) enhance the light–matter coupling. If the coupling strength g remains lower than the QD emission rate into non-collected modes γ and the cavity loss rate κ, the system is in the weak coupling regime where the emission rate is increased by Purcell enhancement and facilitates higher operational rates. Resonators with high Q-factors work only with a narrow bandwidth which is compatible with most schemes for the generation of single photons but may be problematic for the generation of other types of non-classical light. An enhancement of the emission rate reduces the indistinguishability under non-resonant excitation since the timing jitter from the excitation process becomes more important.[84] On the other hand, in schemes with resonant excitation, increasing the emission rate is expected to increase the indistinguishability since the homogeneous linewidth is increased relative to the inhomogeneous broadening due to spectral diffusion.[62] However, it has has also been shown that the proximity to etched surfaces increases spectral diffusion[85] which poses a lower limit on the resonator size. Here, surface passivation techniques may play an important role in the future.[85,86]

Over the years, a wealth of different resonators has been developed. Prominent examples are micropillars, oxide aperture cavities, photonic crystal cavities, bulls-eye resonators, microlenses, tapered nanowires, and tunable Fabry–Perot resonators. In the following, we will first discuss aspects that are relevant for all resonators before we briefly describe the different resonators and highlight recent progress in the individual structures.

For all resonators, the spatial alignment between QD and resonator is important to achieve an efficient coupling between QD and resonator mode.[87] This can be achieved either probabilistically by fabricating a large number of QD–resonator systems and then characterizing them all or deterministically by precharacterizing QDs and then subsequently fabricating resonators around

the precharacterized QDs. Moreover, for high-Q resonators a spectral alignment of QD and resonator mode is essential.[88] Therefore, it is often useful to fine tune the detuning between QD and resonator mode and several techniques have been developed. Prominent examples are temperature tuning,[89–91] electric tuning of the QD emission frequency via the DC stark[92,93] effect or ultrafast tuning via the AC stark effect,[94] deposition of monolayers,[95] or condensation of inert gases[96] on the surface which changes the resonator frequency and strain tuning, either DC[97,98] or dynamically using surface acoustic waves.[99]

When resonant excitation with cross-polarized suppression of the excitation laser is combined with QDs coupled to resonators in the weak coupling regime the emission mainly consist of coherent scattering from the resonator.[100] Therefore, the resonator is not allowed to rotate the polarization of the coherently scattered laser light relative to the excitation laser such that it can be suppressed in the detection channel. Otherwise, the emission would be dominated by coherently scattered laser light and not the quantum light emitted by the QD. On the other hand, the QD emission must be rotated relative to the excitation laser such that it couples to the cross-polarized detection channel. This can be achieved, for example, in bimodal cavities and charge-neutral QDs that have their symmetry axis different from the cavity and laser[101] or bimodal cavities and charged QDs.

3.2.1. Micropillar Resonators

Micropillar resonators consist of a pillar with a typical diameter of a few micrometers.[16,63–68,76,102–109] A λ cavity is sandwiched between bottom and top distributive Bragg reflectors (DBR) whereby the bottom-DBR has a higher number of periods than the top-DBR to make sure that most of the emission leaves the pillar through the top. They are commonly used for efficient single photon generation since they simultaneously offer Purcell enhancement ($F_p \approx 3-10$) and a high collection efficiency. The reported brightness is 0.79 ± 0.08 for non-resonant excitation[105] and 0.37 ± 0.02 for resonant excitation,[64] which is lower due to the polarization filtering of the emission to suppress the excitation laser and damping of the Rabi oscillations which reduces the preparation fidelity of the excited state. Recently, it was demonstrated that elliptical micropillars can reduce the impact of polarization filtering on the brightness by preferentially emitting one polarization that can be aligned with the detection polarization.[110] In order to deterministically align micropillar resonators with QDs an in situ laser lithography technique[103] as well as a technique which is based on imaging of the QD emission[109] have been established. Electrically contacted micropillars were demonstrated[104,106] which further benefit from all the advantages of electrical contacting discussed in Section 2.3 and which were used to demonstrate a very high indistinguishability with $\nu > 0.99$.[65]

3.2.2. Oxide Aperture Cavities

Oxide aperture cavities are a lot like micropillar resonators with the difference that the pillar has a larger diameter of $\approx 30\,\mu\text{m}$.[92,111–120] However, the mode is confined to a diameter similar to micropillars using an oxide aperture above the QD layer resulting in comparable Purcell factors $F_p \approx 2-11$. Electrically contacted oxide aperture cavities have been established in 2007 and reported values of the source brightness are as large as 0.38.[92] Enabled by the large diameter of the pillar a device where fibers are directly attached to the top of the pillar for efficient detection and bottom of the sample for excitation was demonstrated.[119] Thereby, the brightness of the device was 0.05 ± 0.01 photons in the detection fiber per excitation pulse. However, this was limited by a spectral mismatch of QD and resonator and the coupling efficiency between cavity mode and fiber was measured to be 0.85 ± 0.11 and the theoretical maximum was calculated to be 0.9 ± 0.076.

3.2.3. Bulls-Eye Resonators

Bulls-eye resonators are circular DBR resonators which are fabricated by etching circular trenches into a thin membrane.[121–124] The measured Purcell factor of these devices are $F_p \approx 2-4$ while higher factors around $F_p \approx 11-12$ were predicted for perfect spatial and spectral matching of QD and resonator mode. For this alignment, a technique based on imaging of the QD luminescence has been demonstrated.[123–125] The measured brightness is 0.48 ± 0.05 using an numerical aperture of $NA = 0.4$ while a collection efficiency of > 0.8 is predicted for using $NA = 0.9$.

3.2.4. Photonic Crystal Cavities

Photonic crystal cavities consist of a thin membrane which is periodically patterned with air holes and where a deviation from the periodicity results in cavities.[74,75,126–132] Due to their high quality factors and small mode volumes they are well suited for enhancing the light–matter interaction and generating nonclassical light in the weak coupling regime as well as in the strong coupling regime (c.f. Section 3.4). In general, photonic crystal cavities do not have a high collection efficiency since very often a high Q-factor is achieved by reducing the cavity losses through destructive interference in the far field. However, it was recently demonstrated that for the L3 cavity, which consist of three missing air holes in a row in a hexagonal pattern, the higher-order mode M3 has a collection efficiency of 0.443 ± 0.021. Moreover, the planar geometry of photonic crystals makes them ideally suited for coupling to waveguides and on-chip photonic circuits.[127,128,130] To these ends, recently the generation of single photons in a cavity coupled to a waveguide was demonstrated with a very high Purcell enhancement of $F_p = 43 \pm 2$ and high indistinguishability ($\nu = 0.939 \pm 0.033$).[131]

3.2.5. Microlenses

Microlenses are micrometer-sized lenses which are monolithically fabricated into the bulk substrate.[133–140] The reported brightness is 0.23 ± 0.03 using a numerical aperture of $NA = 0.4$ and collection efficiencies > 0.8 are expected using more sophisticated lens designs.[133] Moreover, a collection efficiency of 0.4 ± 0.04 has been demonstrated using the combination of a

monolithic microlens combined with a 3D printed microobjective.[139] Since microlenses are not high-Q resonators which enhance the emission rate they operate broadband. Spatial alignment between QD and lens has been realized using an in situ cathode luminescence imaging and electron beam lithography technique[133,141] as well as in situ optical lithography.[140]

3.2.6. Tapered Nanowires

Tapered nanowires are nanowires which are tapered to adiabatically expand the guided mode toward the top of the nanostructure which results in a high out-coupling and collection efficiency.[43,98,142–145] Similar to microlenses, the absence of a high-Q resonator facilitates broadband operation. The nanowire can either be fabricated top-down[142] or bottom-up during the growth of nanowire QDs[43] whereby the bottom-up process automatically ensures spatial alignment between QD and resonator. Interestingly, the taper can either decrease or increase the width toward the top and the reported brightness is 0.75 ± 0.1.[143]

3.2.7. Tunable Fabry–Perot Resonators

Tunable Fabry–Perot resonators[146–151] consist of two parts: the sample which consist of a planar back DBR as well as a part of the cavity containing the QDs and the curved top DBR which is either fabricated into the tip of a fiber[146,147,151] or a glass template.[148–150] Therefore, they allow to easily tune the resonator frequency by changing the distance between bottom part and top part. Moreover, by moving the bottom part and top part relative to each other in lateral direction, it is possible to spatially align any QD in the bottom part with the resonator mode. Due to the high Q-factor and small mode volume, this type of resonator was recently used to demonstrate strong coupling very far in the strong coupling regime.[150] While efficient single photon generation has not been demonstrated so far, calculations indicate that for lower Q-factor resonators extraction efficiencies > 0.9 are within reach.[150]

3.3. Waveguides

For on-chip applications such as integrated quantum photonic circuits, QDs are often integrated into waveguides rather than cavities.[152–166] Here, photonic crystal W1 waveguides, which consist of one row of missing holes, have been used[152–157,160,161,166] as well as photonic crystal glide-plane waveguides, which allow for a chiral light–matter coupling,[159] and nanobeam waveguides.[158,162–165] Due to the efficient emission of QDs into the waveguide mode high source brightness in the waveguide can be realized. This is quantified by the β-factor which is the ratio of emission into the desired mode compared to all emission and for QDs in photonic crystal waveguides, β-factors as high as $\beta = 98.43 \pm 0.04$ have been observed.[157] The single photons can then be used on-chip, for example, for quantum networks[167] or efficiently coupled to single mode fibers.[161,164] In addition to generating single photons using the schemes discussed above, nonlinear quantum optics can also result in the reflection of a coupled QD–single mode waveguide system to generate single photons through nonlinear quantum optics.[160,165]

3.4. Resonators (Strong Coupling Regime)

Another geometry of interest which promises to allow for the on-chip integration similar to QDs in waveguides while profiting from the advantages of using a resonator is a QD–resonator system coupled to an input waveguide and an output waveguide (**Figure 7**a).

As discussed above, for off-chip applications resonant excitation can be combined with a QD weakly coupled to a resonator if the structure allows that the polarization of the coherent scattering from the resonator is not rotated, such that in can be suppressed in the detection channel, while the polarization of the QD emission is rotated. However, for on-chip applications, where a QD–resonator system is coupled to an input waveguide and an output waveguide (Figure 7a), the transmission would consists mainly of coherently scattered laser instead of single photons. While structures using this on-chip transmission geometry have been investigated most experiments are actually carried out in an off-chip geometry where for a linearly polarized resonator the transmission equivalent to the on-chip geometry is obtained when using cross-polarized resonant excitation and detection with the linearly polarized resonator mode aligned diagonal to the setup polarization axis.

In transmission geometry, single photons can be generated using a strongly coupled QD–cavity system, that is, when the coupling strength g exceeds the QD emission rate into non-collected modes γ and cavity loss rate κ. When QD and cavity are tuned into resonance the eigenstates of the system are polaritons with energies $E_n^{\pm} = n\hbar\omega \pm 2\sqrt{n}\hbar g$ where n is the number of photons involved and which is known as Jaynes–Cummings ladder (JC-ladder). The energy structure as a function of the QD–cavity detuning Δ is visualized in Figure 7b for $n \leq 2$. At resonance, the eigenstates of each rung n are the polaritons which are split by $\sqrt{n}2g$ and with increasing detuning they evolve toward the bare QD and cavity states. The characteristic anticrossing of the lowest rung can be measured using photoluminescence[89–91] or cross-polarized reflectivity[170] as presented in Figure 7c.[169] In this system single photons can be generated through the anharmonicity of the JC-ladder. A laser tuned into resonance with the first rung of the ladder (blue arrow Figure 7c) is not in resonance with subsequent climbs up the ladder. Therefore, the admission of a photon to the system reduces the probability for a second photon to be admitted which is known as photon blockade.[171,172] However, due to the highly dissipative character of nanophotonic systems the observed antibunching for QD and cavity in resonance is moderate.[171,172] Although a laser in resonance with the first rung is not in exact resonance with the transmission from the first rung to the second rung it still has significant overlap with the transition due to the linewidth of the states. In order to increase the anharmonicity and reduce the value of $g^{(2)}[0]$, detuning of QD and cavity can be used.[168] This is visualized in Figure 7d which presents the detuning dependent energy differences between the rungs for transitions leading to $n = 1$, $n = 2$,

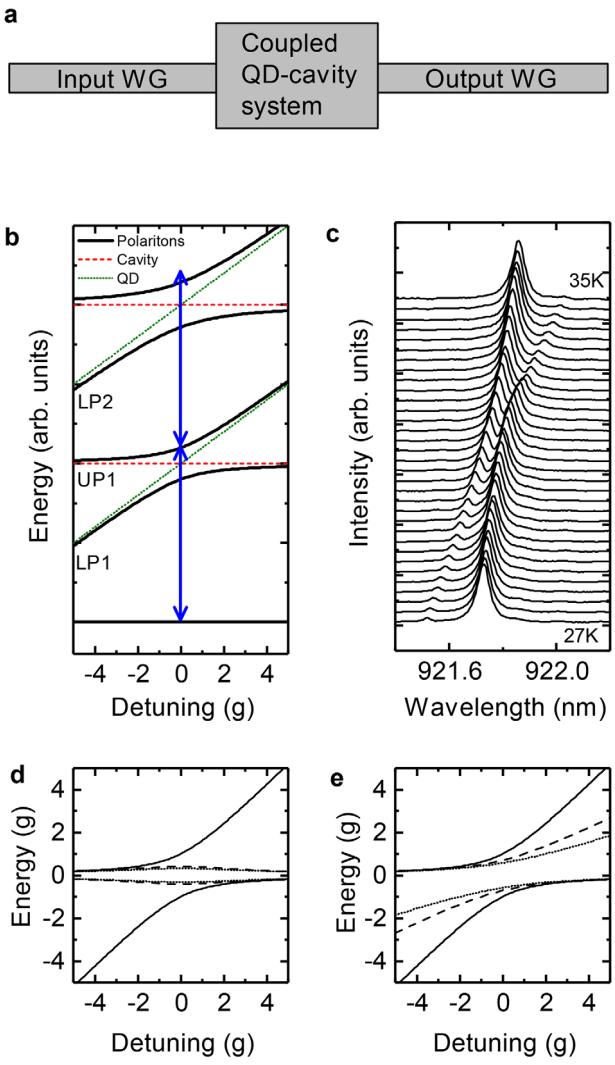

Figure 7. Generation of single photons from strongly coupled systems. a) Illustration of on-chip architecture. b) Schematic illustration of the first two-rungs of the Jaynes–Cummings ladder and visualization of photon blockade. c) Anticrossing of the lowest rung measured in cross-polarized reflectivity. d) Energy of transitions from the ground state to the first rung (solid lines) and subsequent climbs of higher rungs (dashed and dotted lines). e) Energies of exciting the nth rung of the JC-ladder in an n-photon process for $n = 1$ (solid lines), $n = 2$ (dashed lines), and $n = 3$ (dotted lines). In (d) and (e), the energies are given relative to the cavity energy. (b,d,e) Adapted from ref. [168] and (c) adapted from ref. [169] with permission. Copyright 2015, American Physical Society.

$n = 3$ as solid, dashed, and dotted lines, respectively. With increasing QD–cavity detuning the energy difference between transitions to the first rung (solid lines) and higher climbs up the JC-ladder (dashed and dotted lines) increases for exciting the more QD-like polariton. This is also the case for the energies of exciting the nth rung of the JC-ladder in an n-photon process (Figure 7e). In addition, the pulse length of the excitation laser can be optimized:[169] longer excitation pulses increase the chance of re-excitation during the presence of the pulse while shorter pulses have a broader linewidth and thus increase the overlap with the different transitions. Exploiting detuning of QD and cavity and optimizing the pulse length allowed to observe antibunching with $g^{(2)}[0] = 0.34 \pm 0.07$. Importantly, the limiting factor is coherent scattering of the laser from the detuned cavity.[100]

For a photonic crystal cavity system in off-chip geometry this coherent scattering of the laser from the detuned cavity can be interferometrically cancelled using a self-homodyne effect which is intrinsic to photonic crystal cavities.[174] Here, coherently scattered light from the cavity interferes with light scattered from the photonic crystal region outside of the cavity producing a Fano resonance. Consequently, for balancing the relative strength of these two components the coherent scattering of a laser tuned to the dip of the Fano resonance can be entirely suppressed. Combining this effect with the detuned photon blockade discussed above allows to isolate the non-classical light from the otherwise dominating coherently scattered background and has enabled the observation of single-photon generation with $g^{(2)}[0] = 0.05 \pm 0.04$, $\nu = 0.96 \pm 0.05$, and an emission rate of $1/55$ ps^{-1}.[100]

To realize this interferometric cancellation condition in an on-chip transmission geometry a sample design based on an input and output waveguide which are coupled not only to the cavity but also to a partially transmitting element (PTE) can be used (**Figure 8**a).[173] The simulated transmission of such a proposed structure (Figure 8b) is presented in Figure 8c for $\Delta = 6g$ which shows the transmission with the PTE fully blocking (JC-system) and tuned to optimal interferometric cancellation as dashed and solid lines, respectively.[173] Here, a fabricable Q-factor of the cavity of ≈ 51.000 in the absence of the waveguides and an easily achievable coupling strength of $g = 10 \times 2\pi$ GHz have been used.[89,170,171,175] In both cases two peaks are observed—the cavity like polariton at $\approx 0g$ and the QD-like polariton at $\approx 6g$. However, in the case of the PTE fully blocking (red dashed lines) the spectra consists of two Lorentzian peaks while for the system tuned to optimal interferometric cancellation (solid black line) the cavity-like polariton forms a Fano resonance with the QD-like polariton in its dip.

While the difference in the transmission spectra is not very significant, the photon blockade observed for tuning the laser to the more QD-like polariton (small peak at $\approx 6g$ in Figure 8c) is dramatically different for the two conditions. The power dependent $g^{(2)}[0]$ is presented in Figure 8d for the PTE fully blocking and tuned to optimal interferometric cancellation as dashed and solid lines, respectively. While without interferometric cancellation (dashed line) the purity of single-photon generation is moderate ($g^{(2)}[0] \approx 0.1$) with optimal interferometric cancellation (solid line) high-quality single photons with $g^{(2)}[0] < 10^{-4}$ are observed for effective driving strengths < 1 (where 1 corresponds to a pulse area of π). We would like to note here, that this interferometric cancellation of coherent scattering from a detuned cavity is not exclusive to strongly coupled systems but similarly works for weakly coupled systems.[176]

4. Entangled Photon Pairs

Entangled photon pairs are essential for several quantum communication protocols such as the E91 protocol[2] in which an entangled photon pair source (EPS) is used for quantum key distribution (**Figure 9**a). Moreover, they can be used for Bell tests[177] and for quantum teleportation.[178,179]

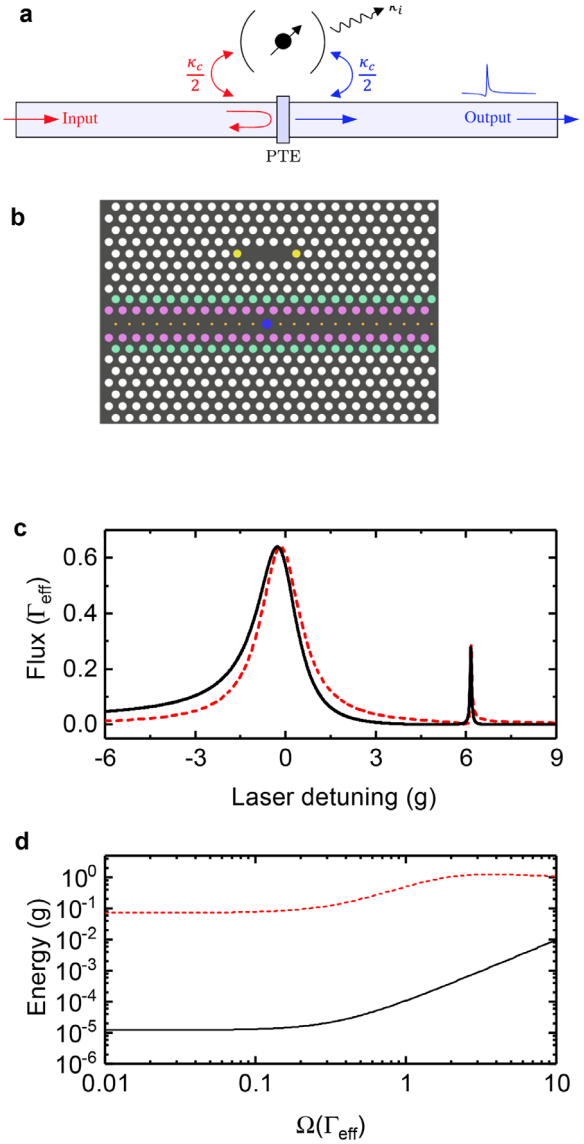

Figure 8. Interferometric cancellation of coherent scattering from the cavity. a) Schematic illustration of a cavity coupled to an input and an output waveguide and where a direct transmission from input to output waveguide can be controlled with a PTE. b) Suggested structure based on a photonic crystal platform. Colored circles indicate holes where the position or size is changed relative to the crystal. c) Transmission of the system for a QD–cavity detuning of $\Delta = 6g$ with the PTE fully blocking (red dashed line) and optimized for interferometric cancellation (black solid line). d) $g^{(2)}[0]$ as a function of the driving strength for the laser in resonance with the more QD-like polariton with the PTE fully blocking (red dashed line) and optimized for interferometric cancellation (black solid line). Adapted with permission.[173] Copyright 2016, American Physical Society.

The EPS emits a pair of entangled photons in one of the four Bell states:

$$|\Phi^+\rangle = \frac{1}{\sqrt{2}}(|H\rangle_A|H\rangle_B + |V\rangle_A|V\rangle_B)$$

$$|\Phi^-\rangle = \frac{1}{\sqrt{2}}(|H\rangle_A|H\rangle_B + |V\rangle_A|V\rangle_B)$$

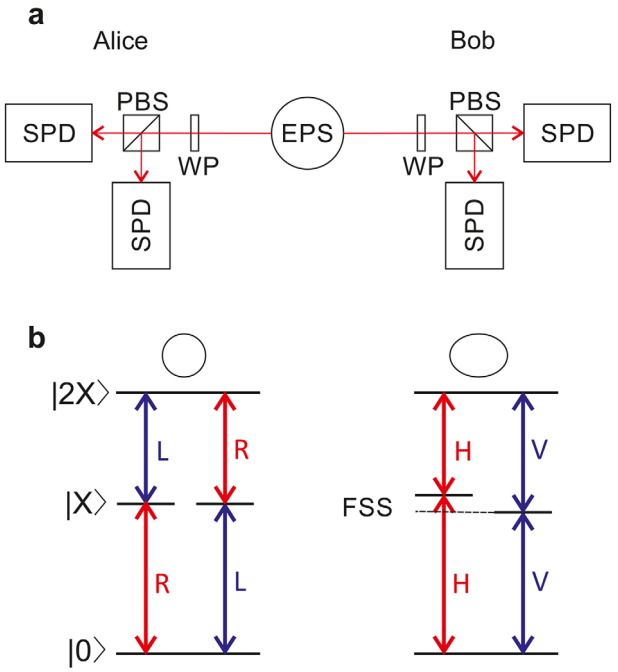

Figure 9. Entangled photon pairs. a) Schematic illustration of a setup for using entangled photons for quantum communication and for quantifying the entanglement. EPS, entangled photon source, SPD, single photon detector, PBS, polarizing beamsplitter, WP, waveplates. b) Schematic illustration of the lowest energy levels of an uncharged QD with (left) and without (right) D_{2D} symmetry.

$$|\Psi^+\rangle = \frac{1}{\sqrt{2}}(|H\rangle_A|V\rangle_B + |H\rangle_A|V\rangle_B)$$

$$|\Psi^-\rangle = \frac{1}{\sqrt{2}}(|H\rangle_A|V\rangle_B - |H\rangle_A|V\rangle_B)$$

where H and V denote the polarization of the photons and the indices the spatial position Alice (A) or Bob (B). When Alice and Bob measure in the same basis the results are perfectly correlated independent of the choice of basis which can be used to generate a secret key and eavesdropping can be detected by tests of Bell's theorem.

For many applications, it is important that the entanglement is of high quality. As was done for a mixed single-photon source, a density matrix can be factorized into a sum of density matrices corresponding to pure states

$$\hat{\rho} = \sum_i \sigma_i |\Psi_i\rangle\langle\Psi_i| \tag{68}$$

where σ_i denotes the portion of an ensemble to be in the state $|\Psi_i\rangle$. For example, the state $|\Psi^+\rangle$ has the density matrix

$$\hat{\rho}_0 = \frac{1}{2}\begin{pmatrix} 1 & 0 & 0 & 1 \\ 0 & 0 & 0 & 0 \\ 0 & 0 & 0 & 0 \\ 1 & 0 & 0 & 1 \end{pmatrix}$$

To experimentally measure the density matrix $\hat{\rho}_{\text{exp}}$, 16 correlation measurements using different bases have to be performed with a setup as schematically illustrated in Figure 9a. The degree of entanglement can then be quantified through several parameters which can be calculated from the deviation of $\hat{\rho}_{\text{exp}}$ from $\hat{\rho}_0$ such as concurrence or negativity.[21] For QDs, a commonly used quantity to compare different sources is the fidelity that can be written as $F = \text{Tr}[\hat{\rho}_{\text{exp}} \cdot \rho_0]$ (which is the inner product of two Hermitian operators associated with the Frobenius norm). Importantly, this quantity can be measured using less than the 16 correlation measurements mentioned above.

In the year 2000, it was proposed that QDs can be used as sources of entangled photon pairs[180] which was for the first time experimentally demonstrated in 2006[181] and over recent years their potential as high-quality sources has been established.[182–203] An important milestone for the generation of entangled photon pairs was the development of two-photon excitation of $|2X\rangle$ either in a resonant two-photon process[71,72] or via a detuned phonon-mediated process[73] which allows for an on-demand generation with high efficiency.[186] The energy level diagram of the lowest energy states of uncharged QDs was already discussed in Section 2.3 and is reproduced in Figure 9b. When preparing a QD with D_{2D} symmetry in the $|2X\rangle$, the radiative decay of the state $|2X\rangle$ will produce a photon which has its polarization entangled with the spin of the state $|X\rangle$. Subsequently, the radiative decay of $|X\rangle$ will transfer the entanglement to the second photon which results in an entangled photon pair which can be written as

$$|\Psi\rangle = \frac{1}{\sqrt{2}}(|R\rangle_{2X}|L\rangle_X + |L\rangle_{2X}|R\rangle_X) \tag{69}$$

Since the energies of the two photons are different, they can be easily separated. However, any realistic QD will not have D_{2D} symmetry but rather some degree of anisotropy which, as discussed in Section 2.3, leads to two non-degenerate $|X\rangle$ states which are split by a finestructure splitting of energy FSS and couple to linearly polarized light. Therefore, the entangled wavefunction will take the form

$$|\Psi(t)\rangle = \frac{1}{\sqrt{2}}(|H\rangle_{2X}|H\rangle_X + e^{i\frac{FSS}{\hbar}t}|V\rangle_{2X}|V\rangle_X) \tag{70}$$

and the overlap with a target Bell state precesses in time. This means that in a pulse-wise integrated form, which is desired for applications, the degree of entanglement degrades. Moreover, single-photon detectors have a limited timing resolution which can make it difficult to resolve the precession.

Consequently, in order to obtain a high degree of entanglement, the finestructure splitting needs to be entirely removed. Removing or reducing the finestructure splitting can be done using the optical Stark effect,[183] a combination of applying strain in the plane of the QDs and vertical electric fields[204,205] as well as by microstructures which can control the amount of strain and direction independently.[190,192,193] Alternatively, QDs which are inherently highly symmetric such as nanowire QDs[185,188,198] or GaAs/AlGaAs QDs grown by droplet epitaxy can be used.[195,197,200,202,206] Using the latter material system entanglement fidelities of up to 0.978(5) have been observed.[200] These QDs also have the additional benefit that their emission wavelengths are suitable for interfacing with atomic vapor quantum memories.[195,197] Recently, in addition to polarization entanglement and time-bin entanglement, hyperentanglement, which is the combination of both, has been demonstrated.[203] Enhancing the extraction efficiency or emission rate is more difficult for entangled photon pairs compared to single photons. Due to the different energies of the $2X$ and X transition, either broadband resonators can be used or resonators that support two modes which are tuned in resonance with the $2X$ and X transitions, respectively.[184] Moreover, for polarization entangled photon pairs, the modes need to be bimodal to support both polarizations which is easier to achieve for low-Q resonators. Remarkably, extraction efficiencies of 0.65 ± 0.04 was recently reported for dielectric antennas.[207]

5. Single Photons Entangled with Spins

QDs deterministically charged with single electrons or holes are also promising as optically-active spin qubits. The stationary spin in the QD can be entangled with the polarization and frequency of a photon and, thus, act as a building block for nodes in quantum networks or for the generation of photonic graph states discussed in Section 6. In a Voigt geometry magnetic field, the ground states and excited states of a charged QD (c.f. Figure 1) are split in energy forming a double lambda system where the vertical transitions couple to vertically polarized light while the diagonal transitions couple to horizontally polarized light. Using just one of the two excited states results in a lambda system where the excited state couples to the two ground states with horizontal and vertical polarization, respectively (c.f. Figure 4e). After initializing a spin either by spin pumping[208,209] or tunneling ionization[210,211] the system can be put in an excited state from where it relaxes to a coherent superposition of the two ground states which is entangled with the energy and polarization of the emitted photon. In addition to the demonstration of spin–photon entanglement[212–214] with over 90% fidelity,[215] the teleportation of a photon polarization into the QD spin[216] and the entanglement between remote electron spins[217] and hole spins[218] has been demonstrated.

For applications in quantum technologies, it is important to quantify the decoherence timescales and to understand the dephasing mechanisms in order to extend achievable coherence times. To these ends a lot of research has been carried out and the main dephasing mechanisms have been identified to be coupling to the nuclear spins as well as charge noise.[219–231] The nuclear spins of the atoms forming the QD are seen by the central spin as a magnetic Overhauser field. Since the dynamics of the nuclear spins are much slower than that of the central electron/hole spin on short timescales the central spin experiences the Overhauser field as frozen. However, in a temporal or spatial ensemble, the Overhauser field is randomly distributed leading to fast dephasing of electron spins with $T_2^* \approx 2$ns.[219,229,231] Due to their p-like central cell wavefunction holes have a weaker hyperfine contact interaction and consequently more than one order of magnitude longer T_2^* have been reported in time domain experiments[232] and in frequency domain measurements (coherent population trapping) for holes T_2^* times approaching one microsecond were

reported.[230] On intermediate timescales of hundreds of ns, the Overhauser field coherently evolves in time due to the quadrupolar moments resulting from the strained nuclei.[229,231] For longer timescales, the mechanism of irreversible dephasing is attributed to nuclear spin co-flips or other complex many-body interaction effects.[220] In spin echo measurements, coherence times of $T_2^{SE} \approx 1-3\mu s$ have been observed for electrons[225,229,231] and holes,[226,232] indicating the presence of charge noise limiting the observed coherence times. To these ends, dynamical decoupling has recently been demonstrated to enhance achievable T_2 times.[232] In addition, it was recently shown that preparing the nuclear spin bath in a subthermal state using optical techniques allows to increase T_2^* by more than one order of magnitude.[233] Moreover, very recently it was demonstrated that an electron spin can be used to coherently manipulate the nuclear spin ensemble opening the path for using it as a long-term quantum memory.[234]

While the coherence times observed with QDs so far are significantly shorter than those observed for example in NV—centers in diamond, due to their superior optical qualities, QDs are still suitable for many applications in quantum technologies. In particular, the spin coherence times are long enough for the generation of photonic graph states as will be discussed in the next section.

6. Photonic Graph States

In quantum information processing and quantum communication, graph states are highly entangled states that can serve as a resource for many information processing tasks. A graph state $|\Psi_G\rangle$ associated with a graph $G = (V, E)$ can be constructed by associating a qubit with every vertex in V and initializing it in the state $|+\rangle = (|0\rangle + |1\rangle)/\sqrt{2}$ followed by an application of a controlled-Z gate between qubits whose corresponding vertices have an edge in E:[235]

$$|\Psi_G\rangle = \prod_{(v_1,v_2)\in E} \mathrm{CZ}^{(v_1,v_2)} |+\rangle^{\otimes V} \tag{71}$$

An alternative and equivalent definition of a graph state is as follows—for every vertex $v \in V$, define an operator $\hat{K}^{(v)}$:

$$\hat{K}^{(v)} = \hat{\sigma}_x^{(v)} \prod_{u\in N_v} \hat{\sigma}_z^{(u)} \tag{72}$$

where N_v is the neighbourhood of v (i.e., $N_v = \{u|\ \exists(u, v) \in E\}$). The graph state $|\Psi_G\rangle$ is then defined as a common eigenvector of $\hat{K}^{(v)}\ \forall\ v \in V$ with unity eigenvalue:

$$\hat{K}^{(v)}|\Psi_G\rangle = |\Psi_G\rangle\ \forall\ v \in V \tag{73}$$

Photonic graph states would refer to such graph states realized with photonic qubits as the physical platform. Most proposals of photonic graph states are based on pulsed polarization qubits—two orthogonal polarizations of light (e.g., horizontal and vertical, right and left circularly polarized) are treated as the $|0\rangle$ and $|1\rangle$ states, with different pulses being treated as different qubits. However, frequency-encoded cluster states have also been proposed.[236]

Graph states have been shown to be an essential resource for measurement based quantum computation[235,237]—in this model of quantum computation, unlike its gate-based counterpart, all the qubits are initialized into a cluster state followed by a sequence of single qubit measurements. A specific quantum algorithm can be obtained by suitably designing the initial graph state and a sequence of such measurements. We note that such a protocol, in general, requires that the future measurements being performed are dependent on the results of the previous measurements and thus relies on a rapid communication of the results of the previous measurements (referred to as "feedforward"[238]). Since the cluster state can potentially be generated by performing two-qubit gates on the emitters being used to generate them, their use for quantum computation obviates the need for design of photonic two qubit gates, which are especially hard to realize due to weak optical nonlinearities.

Apart from quantum computation, graph states are becoming increasingly important in quantum communication. Quantum communication, which refers to the process of transmitting quantum information across a communication channel (e.g., an optical fiber), relies on entanglement between the states of the transmitter and receiver—most quantum communication protocols require a maximally entangled state (e.g., Bell states) to be shared between the two ends of the communication channel.[239] Generating this entanglement over long distances is challenging, and a practical quantum communication system needs refreshment of this entanglement at intermediate nodes referred to as quantum repeaters.[240] The conventional quantum repeater architecture has atomic quantum memories entangled with propagating single-photon wave packets at these intermediate nodes, and a long-distance entanglement of these atomic quantum memories is established by performing a Bell measurement on pairs of the propagating single photons. Such architectures typically require a very large coherence time for the atomic memories, making them infeasible with current technology. As an alternative, all-photonic repeater graph states (RGS) have been proposed.[57] This RGS contains $2m$ photonic qubits out of which m qubits (referred to as the first leaf qubits) form a completely connected graph state, with the remaining m qubits being (referred to as the second leaf qubits) each connected to one of the first leaf qubit. Such an all-photonic state can be used as a building block of a quantum repeater, with the long distance entanglement being created by Bell measurements between second leaf qubits of neighbouring graph states.

Generation of photonic graph states would involve creating entanglements between photonic qubits—this has traditionally been a challenging task since most optical systems are inherently linear. Nonlinearity in optical system can either be introduced through material nonlinearity (e.g., optical nonlinearities such as kerr or $\chi^{(2)}$ nonlinearity, or by coupling the optical field to emitters such as quantum dots), or through photodetection. Photodetection-based graph states are often generated by preparing photon pairs in an entangled (Bell) state via parametric down conversion, followed by a joint detection on photons from different pairs. This photodetection process fuses the entangled pairs together, and different graph states can be designed by controlling the sequence of measurements performed. However, due to the involved photodetection process, this scheme of generating

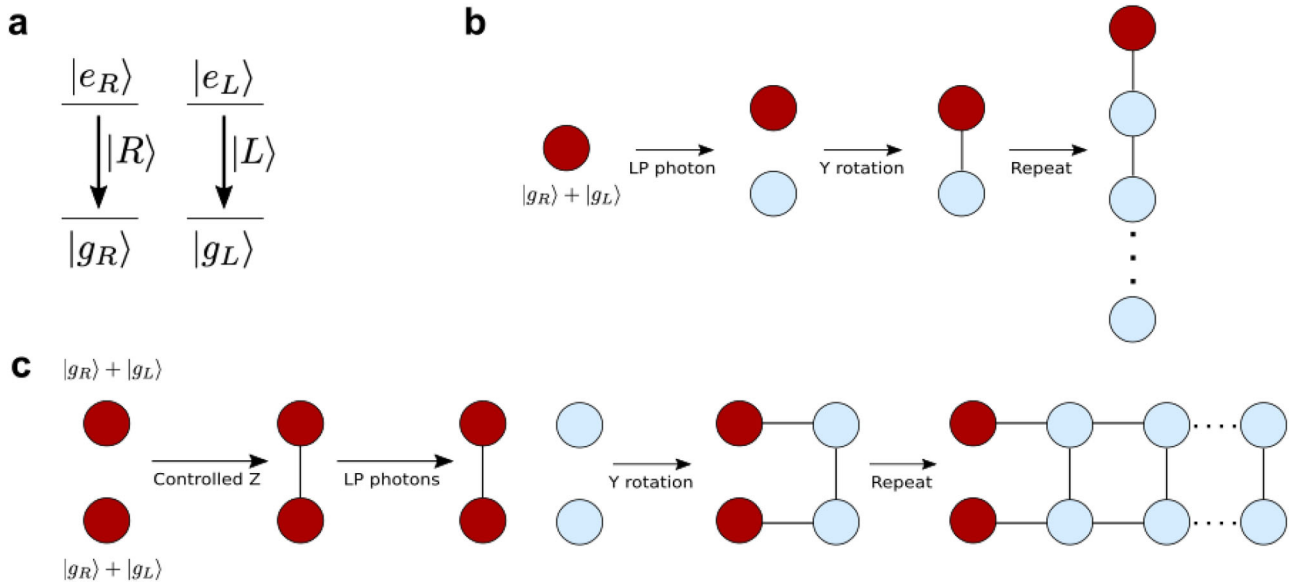

Figure 10. Graph state generation. a) Level structure of an emitter that can be used to generate cluster state—this level structure can be achieved using a singly charged quantum dot as described in Section 2.3. b) Generation of a linear graph state using a single emitter. c) Generation of a 2D ladder graph state using two coupled emitters. In both (b) and (c), red circles denote emitter qubits (with $|g_L\rangle \equiv |0\rangle$ and $|g_R\rangle \equiv |1\rangle$) and blue circles denote photonic qubits (with $|R\rangle \equiv |0\rangle$ and $|L\rangle \equiv |1\rangle$).

graph states is inherently probabilistic and suffers from scalability issues for larger graph states.

Employing emitters to create entanglement between photonic qubits allows us to create a deterministic scheme for generating a given cluster state. The rich level structure of quantum dots and the associated selection rules makes them a potential candidate for entangling photonic qubits. Several proposals for realizing graph states that requires a level structure shown in **Figure 10** have been made in the past decade—this level structure can be obtained in a singly charged quantum dot (Section 2.3). This level structure has two ground states $|g_R\rangle$ and $|g_L\rangle$ that coupled via optical transitions to two excited states $|e_R\rangle$ and $|e_L\rangle$, respectively—the transition from $|g_R\rangle$ to $|e_R\rangle$ couples to a right circularly polarized optical mode and that from $|g_L\rangle$ to $|e_L\rangle$ couples to a left circularly polarized optical mode. Generation of a linear graph state is easily accomplished by applying a sequence of optical excitations and rotations between the two ground states[241]—this is shown in Figure 10b and described below:

1. Initialize the emitter to a (unnormalized) state $|g_R\rangle + |g_L\rangle$ and excite it with a linear polarized single photon. Since a linear polarized photon will be an equal superposition of left- and right-circularly polarized photon, the final entangled state of the photon-emitter system would be $|R\rangle|g_R\rangle + |L\rangle|g_L\rangle$.
2. Apply a $\pi/2$ rotation on the qubit formed by the ground states ($|1\rangle \equiv |g_R\rangle$ and $|0\rangle = |g_L\rangle$) around the y axis to obtain the state $(|g_L\rangle + |g_R\rangle)|R\rangle_1 + (-|g_R\rangle + |g_L\rangle)|L\rangle_1$—this rotation can be easily performed by applying a suitable oriented magnetic field to the quantum dot. At this point, the emitter and the emitted photon already form a linear graph state with two vertices (assuming that $|g_R\rangle$ and $|R\rangle_1$ are interpreted as $|1\rangle$ and $|g_L\rangle$ and $|L\rangle_1$ are interpreted as $|0\rangle$).
3. Scatter another linearly polarized photon from the emitter, followed by another y rotation of the ground state to obtain the linear graph state with 3 vertices. Repeat this step to increase the length of the linear graph state.

Note that the graph state created so far has 1 qubit formed by the ground states of the emitter and the remaining qubits formed by emitted the left- and right-polarized photon. A measurement on the most recently generated photon on the computational basis ($|R\rangle$ and $|L\rangle$) would project the emitter into one of the ground states and the remaining photons into a (smaller) linear graph state.

This proposal can be adapted to generate 2D cluster states by employing coupled emitters as delineated in ref. [242]. Figure 10c diagramatically shows the generation of such a cluster state. Both emitters are initialized to an equal superposition of the two ground states $((|g_R\rangle_1 + |g_L\rangle_1) \otimes (|g_R\rangle_2 + |g_L\rangle_2))$, followed by an application of the controlled-Z gate between the two emitters. This effectively creates a two-qubit graph state between the two emitters $|g_R\rangle_1|g_R\rangle_2 - |g_R\rangle_1|g_L\rangle_2 + |g_L\rangle_1|g_R\rangle_2 + |g_L\rangle_1|g_L\rangle_2)$. It was proposed that the CZ gate can be realized by optically coupling the trion states of the quantum dots, which lie above $|e_R\rangle$ and $|e_L\rangle$ in the energy spectrum.[243] Next, we scatter a linearly polarized photon off each emitter. After the completion of the scattering process, the emitters and photons would be in an entangled state $|g_R\rangle_1|R\rangle_1|g_R\rangle_2|R\rangle_2 - |g_R\rangle_1|R\rangle_1|g_L\rangle_2|L\rangle_2 + |g_L\rangle_1|L\rangle_1|g_R\rangle_2|R\rangle_2 + |g_L\rangle_1|L\rangle_1|g_L\rangle_2|L\rangle_2$. Note that this is still a two qubit graph state with $|1\rangle \equiv |g_R\rangle|R\rangle$ and $|0\rangle \equiv |g_L\rangle|L\rangle$. Application of a $\pi/2$ rotation along y-axis on the qubit formed by $|g_R\rangle$ and $|g_L\rangle$ for both the emitters results in a square graph state between the four qubits (two emitter qubits and two photonic qubits). Repeating this step increases the length of the graph state, resulting a ladder graph state. A similar

strategy of applying controlled-Z gates in between two emitters followed by scattering of single photons together with the local complementation[244] property of graph states can be used to deterministically generate more complicated graph states.[245,246]

Recently, for the first time, the generation of a 1D graph state using semiconductor QDs has been demonstrated[247]—the experiment clearly demonstrated the versatility of quantum dots as an emitter for producing such entangled states. Implementation of the generation of 2D cluster states with quantum dot molecules is a promising direction of research, with the primary challenge being experimentally tuning the quantum dots into resonance with each other and implementing a controlled gate between them. Dephasing errors also present a major obstacle in the generation of cluster states.[248] Moreover, efficient characterization of the entanglement in large cluster states[249,250] which does not rely on a complete state tomography is also an active area of research and would likely yield characterization tools that would help improve the fidelity of cluster state generation.

7. Conclusion

In summary, this Review discussed the generation of non-classical light using semiconductor quantum dots. We discussed the underlying fundamentals, including a thorough theoretical description of quantum light and light–matter interaction and summarized recent progress in the generation of single photons, entangled photon pairs, and cluster states. This field has made an enormous progress over the past few years and high-quality sources of non-classical light based on semiconductor quantum dots have been demonstrated using many different approaches. Therefore, we expect that these sources will play a pivotal role in fundamental quantum physics research as well as quantum technology applications in the near future.

Supporting Information

Supporting Information is available from the Wiley Online Library or from the author.

Acknowledgements

The authors gratefully acknowledge financial support from the German Federal Ministry of Education and Research via the funding program Photonics Research Germany (contract number 13N14846), the European Union's Horizon 2020 research and innovation programme under grant agreement No. 820423 (S2QUIP), the Deutsche Forschungsgemeinschaft (DFG, German Research Foundation) under Germany's Excellence Strategy, EXC-2111-390814868, the Bavarian Academy of Sciences and Humanities, and the National Science Foundation grant ECCS 1839056. R.T. acknowledges funding from Kailath Stanford Graduate Fellowship.

Conflict of Interest

The authors declare no conflict of interest.

Keywords

entanglement, non-classical light, quantum communication, quantum dots, quantum optics, quantum photonics, single photons

Received: January 16, 2019
Revised: October 1, 2019
Published online: December 17, 2019

[1] C. H. Bennett, G. Brassard, *Proc. of the IEEE Int. Conf. on Computers, Systems and Signal Processing*, IEEE, Bangalore, India **1984**.
[2] A. K. Ekert, *Phys. Rev. Lett.* **1991**, *67*, 661.
[3] E. Knill, R. Laflamme, G. J. Milburn, *Nature* **2001**, *409*, 46.
[4] N. Gisin, G. Ribordy, W. Tittel, H. Zbinden, *Rev. Mod. Phys.* **2002**, *74*, 145.
[5] V. Giovannetti, S. Lloyd, L. Maccone, *Science* **2004**, *306*, 1330.
[6] N. Gisin, R. Thew, *Nat. Photonics* **2007**, *1*, 165.
[7] J. L. O'Brien, *Science* **2007**, *318*, 1567.
[8] P. Kok, W. J. Munro, K. Nemoto, T. C. Ralph, J. P. Dowling, G. J. Milburn, *Rev. Mod. Phys.* **2007**, *79*, 135.
[9] A. P. Lund, A. Laing, S. Rahimi-Keshari, T. Rudolph, J. L. O'Brien, T. C. Ralph, *Phys. Rev. Lett.* **2014**, *113*, 100502.
[10] *Quantum Dots for Quantum Information Technologies* (Ed.: P. Michler), Springer, New York **2017**.
[11] C. Matthiesen, A. N. Vamivakas, M. Atatüre, *Phys. Rev. Lett.* **2012**, *108*, 093602.
[12] J. H. Prechtel, A. V. Kuhlmann, J. Houel, L. Greuter, A. Ludwig, D. Reuter, A. D. Wieck, R. J. Warburton, *Phys. Rev. X* **2013**, *3*, 041006.
[13] J. Hansom, C. H. Schulte, C. Matthiesen, M. J. Stanley, M. Atature, *Appl. Phys. Lett.* **2014**, *105*, 172107.
[14] A. V. Kuhlmann, J. H. Prechtel, J. Houel, A. Ludwig, D. Reuter, A. D. Wieck, R. J. Warburton, *Nat. Commun.* **2015**, *6*, 8204.
[15] R. J. Warburton, C. Schäflein, D. Haft, F. Bickel, A. Lorke, K. Karrai, J. M. Garcia, W. Schoenfeld, P. M. Petroff, *Nature* **2000**, *405*, 926.
[16] M. Pelton, C. Santori, J. Vučković, B. Zhang, G. S. Solomon, J. Plant, Y. Yamamoto, *Phys. Rev. Lett.* **2002**, *89*, 233602.
[17] J. C. Loredo, M. A. Broome, P. Hilaire, O. Gazzano, I. Sagnes, A. Lemaitre, M. P. Almeida, P. Senellart, A. G. White, *Phys. Rev. Lett.* **2017**, *118*, 130503.
[18] H. Wang, Y. He, Y.-H. Li, Z.-E. Su, B. Li, H.-L. Huang, X. Ding, M.-C. Chen, C. Liu, J. Qin, J.-P. Li, Y.-M. He, C. Schneider, M. Kamp, C.-Z. Peng, S. Höfling, C.-Y. Lu, J.-W. Pan, *Nat. Photonics* **2017**, *11*, 361.
[19] I. Aharonovich, D. Englund, M. Toth, *Nat. Photonics* **2016**, *10*, 631.
[20] P. Senellart, G. Solomon, A. White, *Nat. Nanotechnol.* **2017**, *12*, 1026.
[21] A. Orieux, M. A. M. Versteegh, K. D. Jöns, S. Ducci, *Rep. Prog. Phys.* **2017**, *80*, 076001.
[22] D. Huber, M. Reindl, J. Aberl, A. Rastelli, R. Trotta, *J. Opt.* **2018**, *20*, 073002.
[23] P. Lodahl, S. Mahmoodian, S. Stobbe, *Rev. Mod. Phys.* **2015**, *87*, 347.
[24] P. Lodahl, *Quantum Sci. Technol.* **2018**, *3*, 013001.
[25] S. Dutra, G. Nienhuis, *J. Opt. B: Quantum Semiclassical Opt.* **2000**, *2*, 584.
[26] H. Carmichael, *An Open Systems Approach to Quantum Optics: Lectures Presented at The Université Libre de Bruxelles, October 28 to November 4, 1991*, Vol. 18, Springer Science & Business Media, Berlin **2009**.
[27] L. Lamata, J. León, *J. Opt. B: Quantum Semiclassical Opt.* **2005**, *7*, 224.
[28] L. De Santis, G. Coppola, C. Antón, N. Somaschi, C. Gómez, A. Lemaître, I. Sagnes, L. Lanco, J. Loredo, O. Krebs, P. Senellart, *Phys. Rev. A* **2019**, *99*, 022312.
[29] K. A. Fischer, L. Hanschke, J. Wierzbowski, T. Simmet, C. Dory, J. J. Finley, J. Vučković, K. Müller, *Nat. Phys.* **2017**, *13*, 649.
[30] K. A. Fischer, R. Trivedi, V. Ramasesh, I. Siddiqi, J. Vučković, *Quantum* **2018**, *2*, 69.
[31] R. Loudon, *The Quantum Theory of Light*, Oxford University Press, Oxford **2000**.

[32] L. Hanschke, *npj Quantum Inf.* **2018**, *4*, 43.
[33] Y. Arakawa, H. Sakaki, *Appl. Phys. Lett.* **1982**, *40*, 939.
[34] R. Enzmann, M. Bareiss, D. Baierl, N. Hauke, G. Böhm, R. Meyer, J. Finley, M.-C. Amann, *J. Cryst. Growth* **2010**, *312*, 2300.
[35] M. Benyoucef, M. Yacob, J. P. Reithmaier, J. Kettler, P. Michler, *Appl. Phys. Lett.* **2013**, *103*, 162101.
[36] T. Miyazawa, K. Takemoto, Y. Nambu, S. Miki, T. Yamashita, H. Terai, M. Fujiwara, M. Sasaki, Y. Sakuma, M. Takatsu, T. Yamamoto, Y. Arakawa, *Appl. Phys. Lett.* **2016**, *109*, 132106.
[37] M. Paul, F. Olbrich, J. Höschele, S. Schreier, J. Kettler, S. L. Portalupi, M. Jetter, P. Michler, *Appl. Phys. Lett.* **2017**, *111*, 033102.
[38] C. Heyn, A. Stemmann, T. Köppen, C. Strelow, T. Kipp, M. Grave, S. Mendach, W. Hansen, *Appl. Phys. Lett.* **2009**, *94*, 183113.
[39] D. Sonnenberg, A. Graf, V. Paulava, W. Hansen, C. Heyn, *Appl. Phys. Lett.* **2012**, *101*, 143106.
[40] C. Heyn, M. Zocher, L. Pudewill, H. Runge, A. Kuster, W. Hansen, *J. Appl. Phys.* **2017**, *121*, 044306.
[41] J. Skiba-Szymanska, R. M. Stevenson, C. Varnava, M. Felle, J. Huwer, T. Müller, A. J. Bennett, J. P. Lee, I. Farrer, A. B. Krysa, P. Spencer, L. E. Goff, D. A. Ritchie, J. Heffernan, A. J. Shields, *Phys. Rev. Applied* **2017**, *8*, 014013.
[42] G. Juska, V. Dimastrodonato, L. O. Mereni, A. Gocalinska, E. Pelucchi, *Nat. Photonics* **2013**, *7*, 527.
[43] M. E. Reimer, G. Bulgarini, N. Akopian, M. Hocevar, M. B. Bavinck, M. A. Verheijen, E. P. A. M. Bakkers, L. P. Kouwenhoven, V. Zwiller, *Nat. Commun.* **2012**, *3*, 737.
[44] Y. H. Huo, B. J. Witek, S. Kumar, J. R. Cardenas, J. X. Zhang, N. Akopian, R. Singh, E. Zallo, R. Grifone, D. Kriegner, R. Trotta, F. Ding, J. Stangl, V. Zwiller, G. Bester, A. Rastelli, O. G. Schmidt, *Nat. Phys.* **2013**, *10*, 46.
[45] M. Bayer, G. Ortner, O. Stern, A. Kuther, A. A. Gorbunov, A. Forchel, P. Hawrylak, S. Fafard, K. Hinzer, T. L. Reinecke, S. N. Walck, J. P. Reithmaier, F. Klopf, F. Schäfer, *Phys. Rev. B* **2002**, *65*, 195315.
[46] Y. Benny, S. Khatsevich, Y. Kodriano, E. Poem, R. Presman, D. Galushko, P. M. Petroff, D. Gershoni, *Phys. Rev. Lett.* **2011**, *106*, 040504.
[47] A. C. Dada, T. S. Santana, R. N. Malein, A. Koutroumanis, Y. Ma, J. M. Zajac, J. Y. Lim, J. D. Song, B. D. Gerardot, *Optica* **2016**, *3*, 493.
[48] C. Cohen-Tannoudji, J. Dupont-Roc, G. Grynberg, *Atom–Photon Interactions: Basic Processes and Applications*, Wiley-VCH, Weinheim **2004**.
[49] H. J. Carmichael, *Statistical Methods in Quantum Optics 2: Non-Classical Fields*, Springer Science & Business Media, Berlin, Germany **2009**.
[50] K. A. Fischer, K. Müller, K. G. Lagoudakis, J. Vučković, *New J. Phys.* **2016**, *18*, 113053.
[51] R. Trivedi, K. Fischer, S. Xu, S. Fan, J. Vučković, *Phys. Rev. B* **2018**, *98*, 144112.
[52] S. Xu, S. Fan, *Phys. Rev. A* **2015**, *91*, 043845.
[53] L. Mandel, E. Wolf, *Optical Coherence and Quantum Optics*, Cambridge University Press, Cambridge, MA **1995**.
[54] K. A. Fischer, R. Trivedi, D. Lukin, *Phys. Rev. A* **2018**, *98*, 023853.
[55] S. Aaronson, A. Arkhipov, *Proc. of the forty-third annual ACM Symp. on Theory of Computing*, Association for Computing Machinery, San Jose, CA **2011**.
[56] S. Aaronson, *Proc. R. Soc. A* **2011**, *467*, 3393.
[57] K. Azuma, K. Tamaki, H.-K. Lo, *Nat. Commun.* **2015**, *6*, 6787.
[58] Y. Pilnyak, N. Aharon, D. Istrati, E. Megidish, A. Retzker, H. S. Eisenberg, *Phys. Rev. A* **2017**, *95*, 022304.
[59] P. Michler, A. Kiraz, C. Becher, W. V. Schoenfeld, P. M. Petroff, L. Zhang, E. Hu, A. Imamoglu, *Science* **2000**, *290*, 2282.
[60] C. Santori, M. Pelton, G. Solomon, Y. Dale, Y. Yamamoto, *Phys. Rev. Lett.* **2001**, *86*, 1502.
[61] E. B. Flagg, S. V. Polyakov, T. Thomay, G. S. Solomon, *Phys. Rev. Lett.* **2012**, *109*, 163601.
[62] Y.-M. He, Y. He, Y.-J. Wei, D. Wu, M. Atature, C. Schneider, S. Hofling, M. Kamp, C.-Y. Lu, J.-W. Pan, *Nat. Nano* **2013**, *8*, 213.
[63] S. Unsleber, C. Schneider, S. Maier, Y.-M. He, S. Gerhardt, C.-Y. Lu, J.-W. Pan, M. Kamp, S. Höfling, *Opt. Express* **2015**, *23*, 32977, 1512.01048.
[64] S. Unsleber, Y.-M. He, S. Gerhardt, S. Maier, C.-Y. Lu, J.-W. Pan, N. Gregersen, M. Kamp, C. Schneider, S. Höfling, *Opt. Express* **2016**, *24*, 8539.
[65] N. Somaschi, V. Giesz, L. De Santis, J. C. Loredo, M. P. Almeida, G. Hornecker, S. L. Portalupi, T. Grange, C. Antón, J. Demory, C. Gómez, I. Sagnes, N. D. Lanzillotti-Kimura, A. Lemaítre, A. Auffeves, A. G. White, L. Lanco, P. Senellart, *Nat. Photon.* **2016**, *10*, 340.
[66] X. Ding, Y. He, Z.-C. Duan, N. Gregersen, M.-C. Chen, S. Unsleber, S. Maier, C. Schneider, M. Kamp, S. Höfling, C.-Y. Lu, J.-W. Pan, *Phys. Rev. Lett.* **2016**, *116*, 020401.
[67] H. Wang, Z. C. Duan, Y. H. Li, S. Chen, J. P. Li, Y. M. He, M. C. Chen, Y. He, X. Ding, C. Z. Peng, C. Schneider, M. Kamp, S. Höfling, C. Y. Lu, J. W. Pan, *Phys. Rev. Lett.* **2016**, *116*, 213601.
[68] J. C. Loredo, N. A. Zakaria, N. Somaschi, C. Anton, L. De Santis, V. Giesz, T. Grange, M. A. Broome, O. Gazzano, G. Coppola, I. Sagnes, A. Lemaitre, A. Auffeves, P. Senellart, M. P. Almeida, A. G. White, *Optica* **2016**, *3*, 433.
[69] K. A. Fischer, L. Hanschke, M. Kremser, J. J. Finley, K. Müller, J. Vučković, *Quantum Sci. Technol.* **2017**, *3*, 014006.
[70] L. Schweickert, K. D. Jöns, K. D. Zeuner, S. F. C. da Silva, H. Huang, T. Lettner, M. Reindl, J. Zichi, R. Trotta, A. Rastelli, V. Zwiller, *Appl. Phys. Lett.* **2018**, *112*, 093106.
[71] K. Brunner, G. Abstreiter, G. Böhm, G. Tränkle, G. Weimann, *Phys. Rev. Lett.* **1994**, *73*, 1138.
[72] H. Jayakumar, A. Predojević, T. Huber, T. Kauten, G. S. Solomon, G. Weihs, *Phys. Rev. Lett.* **2013**, *110*, 135505.
[73] P. L. Ardelt, L. Hanschke, K. A. Fischer, K. Müller, A. Kleinkauf, M. Koller, A. Bechtold, T. Simmet, J. Wierzbowski, H. Riedl, G. Abstreiter, J. J. Finley, *Phys. Rev. B* **2014**, *90*, 241404.
[74] T. M. Sweeney, S. G. Carter, A. S. Bracker, M. Kim, C. S. Kim, L. Yang, P. M. Vora, P. G. Brereton, E. R. Cleveland, D. Gammon, *Nat. Photonics* **2014**, *8*, 442.
[75] B. C. Pursley, S. G. Carter, M. K. Yakes, A. S. Bracker, D. Gammon, *Nat. Commun.* **2018**, *9*, 115.
[76] J. P. Lee, A. J. Bennett, R. M. Stevenson, D. J. P. Ellis, I. Farrer, D. A. Ritchie, A. J. Shields, *Quantum Sci. Technol.* **2018**, *3*, 024008.
[77] L. Béguin, J.-P. Jahn, J. Wolters, M. Reindl, Y. Huo, R. Trotta, A. Rastelli, F. Ding, O. G. Schmidt, P. Treutlein, R. J. Warburton, *Phys. Rev. B* **2018**, *97*, 205304.
[78] L. Besombes, K. Kheng, L. Marsal, H. Mariette, *Phys. Rev. B* **2001**, *63*, 155307.
[79] I. Favero, G. Cassabois, R. Ferreira, D. Darson, C. Voisin, J. Tignon, C. Delalande, G. Bastard, P. Roussignol, J. M. Gérard, *Phys. Rev. B* **2003**, *68*, 233301.
[80] E. Peter, J. Hours, P. Senellart, A. Vasanelli, A. Cavanna, J. Bloch, J. M. Gérard, *Phys. Rev. B* **2004**, *69*, 041307.
[81] E. A. Muljarov, R. Zimmermann, *Phys. Rev. Lett.* **2004**, *93*, 237401.
[82] A. J. Ramsay, A. V. Gopal, E. M. Gauger, A. Nazir, B. W. Lovett, A. M. Fox, M. S. Skolnick, *Phys. Rev. Lett.* **2010**, *104*, 017402.
[83] D. P. S. McCutcheon, A. Nazir, *New J. Phys.* **2010**, *12*, 113042.
[84] A. Kiraz, M. Atatüre, A. Imamoğlu, *Phys. Rev. A* **2004**, *69*, 032305.
[85] J. Liu, K. Konthasinghe, M. Davanço, J. Lawall, V. Anant, V. Verma, R. Mirin, S. W. Nam, J. D. Song, B. Ma, Z. S. Chen, H. Q. Ni, Z. C. Niu, K. Srinivasan, *Phys. Rev. Applied* **2018**, *9*, 064019.
[86] B. Guha, F. Marsault, F. Cadiz, L. Morgenroth, V. Ulin, V. Berkovitz, A. Lemaître, C. Gomez, A. Amo, S. Combrié, B. Gérard, G. Leo, I. Favero, *Optica* **2017**, *4*, 218.

[87] K. Hennessy, A. Badolato, P. Petroff, E. Hu, *Photonic. Nanostruct.* **2004**, *2*, 65.
[88] A. Badolato, K. Hennessy, M. Atatüre, J. Dreiser, E. Hu, P. M. Petroff, A. Imamoğlu, *Science* **2005**, *308*, 1158.
[89] T. Yoshie, A. Scherer, J. Hendrickson, G. Khitrova, H. M. Gibbs, G. Rupper, C. Ell, O. B. Shchekin, D. G. Deppe, *Nature* **2004**, *432*, 200.
[90] J. P. Reithmaier, G. Sek, A. Loffler, C. Hofmann, S. Kuhn, S. Reitzenstein, L. V. Keldysh, V. D. Kulakovskii, T. L. Reinecke, A. Forchel, *Nature* **2004**, *432*, 197.
[91] E. Peter, P. Senellart, D. Martrou, A. Lemaître, J. Hours, J. M. Gérard, J. Bloch, *Phys. Rev. Lett.* **2005**, *95*, 067401.
[92] S. Strauf, N. G. Stoltz, M. T. Rakher, L. A. Coldren, P. M. Petroff, D. Bouwmeester, *Nat. Photonics* **2007**, *1*, 704.
[93] A. Laucht, F. Hofbauer, N. Hauke, J. Angele, S. Stobbe, M. Kaniber, G. Böhm, P. Lodahl, M.-C. Amann, J. J. Finley, *New J. Phys.* **2009**, *11*, 023034.
[94] R. Bose, T. Cai, G. S. Solomon, E. Waks, *Appl. Phys. Lett.* **2012**, *100*, 231107.
[95] S. Strauf, M. T. Rakher, I. Carmeli, K. Hennessy, C. Meier, A. Badolato, M. J. A. DeDood, P. M. Petroff, E. L. Hu, E. G. Gwinn, D. Bouwmeester, *Appl. Phys. Lett.* **2006**, *88*, 043116.
[96] S. Mosor, J. Hendrickson, B. C. Richards, J. Sweet, G. Khitrova, H. M. Gibbs, T. Yoshie, A. Scherer, O. B. Shchekin, D. G. Deppe, *Appl. Phys. Lett.* **2005**, *87*, 141105.
[97] S. Sun, H. Kim, G. S. Solomon, E. Waks, *Appl. Phys. Lett.* **2013**, *103*, 151102.
[98] P. E. Kremer, A. C. Dada, P. Kumar, Y. Ma, S. Kumar, E. Clarke, B. D. Gerardot, *Phys. Rev. B* **2014**, *90*, 201408.
[99] D. A. Fuhrmann, S. M. Thon, H. Kim, D. Bouwmeester, P. M. Petroff, A. Wixforth, H. J. Krenner, *Nat. Photonics* **2011**, *5*, 605.
[100] K. Müller, K. A. Fischer, C. Dory, T. Sarmiento, K. G. Lagoudakis, A. Rundquist, Y. A. Kelaita, J. Vučković, *Optica* **2016**, *3*, 931.
[101] V. Giesz, N. Somaschi, G. Hornecker, T. Grange, B. Reznychenko, L. De Santis, J. Demory, C. Gomez, I. Sagnes, A. Lemaitre, O. Krebs, N. D. Lanzillotti-Kimura, L. Lanco, A. Auffeves, P. Senellart, *Nat. Commun.* **2016**, *7*, 11986.
[102] C. Santori, D. Fattal, J. Vučković, G. S. Solomon, Y. Yamamoto, *Nature* **2002**, *419*, 594.
[103] A. Dousse, L. Lanco, J. Suffczyński, E. Semenova, A. Miard, A. Lemaître, I. Sagnes, C. Roblin, J. Bloch, P. Senellart, *Phys. Rev. Lett.* **2008**, *101*, 267404.
[104] T. Heindel, C. Schneider, M. Lermer, S. H. Kwon, T. Braun, S. Reitzenstein, S. Höfling, M. Kamp, A. Forchel, *Appl. Phys. Lett.* **2010**, *96*, 011107.
[105] O. Gazzano, S. M. De Vasconcellos, C. Arnold, A. Nowak, E. Galopin, I. Sagnes, L. Lanco, A. Lemaître, P. Senellart, *Nat. Commun.* **2013**, *4*, 1425.
[106] A. K. Nowak, S. L. Portalupi, V. Giesz, O. Gazzano, C. Dal Savio, P. F. Braun, K. Karrai, C. Arnold, L. Lanco, I. Sagnes, A. Lemaître, P. Senellart, *Nat. Commun.* **2014**, *5*, 3240.
[107] V. Giesz, S. L. Portalupi, T. Grange, C. Antón, L. De Santis, J. Demory, N. Somaschi, I. Sagnes, A. Lemaître, L. Lanco, A. Auffèves, P. Senellart, *Phys. Rev. B* **2015**, *92*, 161302.
[108] A. Schlehahn, A. Thoma, P. Munnelly, M. Kamp, S. Höfling, T. Heindel, C. Schneider, S. Reitzenstein, *APL Photonics* **2016**, *1*, 011301.
[109] Y.-M. He, J. Liu, S. Maier, M. Emmerling, S. Gerhardt, M. Davanco, K. Srinivasan, C. Schneider, S. Höfling, *Optica* **2017**, *4*, 802.
[110] Y.-M. He, H. Wang, S. Gerhardt, K. Winkler, J. Jurkat, Y. Yu, M.-C. Chen, X. Ding, S. Chen, J. Qian, Z.-C. Duan, J.-P. Li, L.-J. Wang, S. Y. Yong-Heng Huo, S. Höfling, C.-Y. Lu, J.-W. Pan, arXiv:1809.10992, **2018**.
[111] N. G. Stoltz, M. Rakher, S. Strauf, A. Badolato, D. D. Lofgreen, P. M. Petroff, L. A. Coldren, D. Bouwmeester, *Appl. Phys. Lett.* **2005**, *87*, 031105.
[112] M. T. Rakher, N. G. Stoltz, L. A. Coldren, P. M. Petroff, D. Bouwmeester, *Phys. Rev. Lett.* **2009**, *102*, 097403.
[113] C. Bonato, J. Gudat, K. De Vries, S. M. Thon, H. Kim, P. M. Petroff, M. P. van Exter, D. Bouwmeester, *Opt. Lett.* **2012**, *37*, 4678.
[114] M. P. Bakker, D. J. Suntrup, H. Snijders, T.-A. Truong, P. M. Petroff, D. Bouwmeester, M. P. van Exter, *Opt. Lett.* **2013**, *38*, 3308.
[115] M. P. Bakker, A. V. Barve, A. Zhan, L. A. Coldren, M. P. van Exter, D. Bouwmeester, *Appl. Phys. Lett.* **2014**, *104*, 151109.
[116] M. P. Bakker, A. V. Barve, T. Ruytenberg, W. Löffler, L. A. Coldren, D. Bouwmeester, M. P. van Exter, *Phys. Rev. B* **2015**, *91*, 115319.
[117] M. P. Bakker, H. Snijders, W. Löffler, A. V. Barve, L. A. Coldren, D. Bouwmeester, M. P. van Exter, *Opt. Lett.* **2015**, *40*, 3173.
[118] H. Snijders, J. A. Frey, J. Norman, M. P. Bakker, E. C. Langman, A. Gossard, J. E. Bowers, M. P. van Exter, D. Bouwmeester, W. Löffler, *Nat. Commun.* **2016**, *7*, 12578.
[119] H. Snijders, J. A. Frey, J. Norman, V. P. Post, A. C. Gossard, J. E. Bowers, M. P. van Exter, W. Löffler, D. Bouwmeester, *Phys. Rev. Applied* **2018**, *9*, 031002.
[120] H. J. Snijders, J. A. Frey, J. Norman, H. Flayac, V. Savona, A. C. Gossard, J. E. Bowers, M. P. van Exter, D. Bouwmeester, W. Löffler, *Phys. Rev. Lett.* **2018**, *121*, 043601.
[121] M. Davanco, M. T. Rakher, D. Schuh, A. Badolato, K. Srinivasan, *Appl. Phys. Lett.* **2011**, *99*, 041102.
[122] S. Ates, L. Sapienza, M. Davanco, A. Badolato, K. Srinivasan, *IEEE J. Sel. Top. Quantum Electron.* **2012**, *18*, 1711.
[123] L. Sapienza, M. Davanco, A. Badolato, K. Srinivasan, *Nat. Commun.* **2015**, *6*, 7833.
[124] L. Sapienza, J. Liu, J. D. Song, S. Fält, W. Wegscheider, A. Badolato, K. Srinivasan, *Sci. Rep.* **2017**, *7*, 6205.
[125] J. Liu, M. I. Davanco, L. Sapienza, K. Konthasinghe, J. V. De Miranda Cardoso, J. D. Song, A. Badolato, K. Srinivasan, *Rev. Sci. Instrum.* **2017**, *88*, 023116.
[126] D. Englund, D. Fattal, E. Waks, G. Solomon, B. Zhang, T. Nakaoka, Y. Arakawa, Y. Yamamoto, J. Vučković, *Phys. Rev. Lett.* **2005**, *95*, 013904.
[127] A. Faraon, E. Waks, D. Englund, I. Fushman, J. Vučković, *Appl. Phys. Lett.* **2007**, *90*, 073102.
[128] A. Faraon, A. Majumdar, D. Englund, E. Kim, M. Bajcsy, J. Vučković, *New J. Phys.* **2011**, *13*, 055025.
[129] K. H. Madsen, S. Ates, J. Liu, A. Javadi, S. M. Albrecht, I. Yeo, S. Stobbe, P. Lodahl, *Phys. Rev. B* **2014**, *90*, 155303.
[130] C. Bentham, I. E. Itskevich, R. J. Coles, B. Royall, E. Clarke, J. O'Hara, N. Prtljaga, A. M. Fox, M. S. Skolnick, L. R. Wilson, *Appl. Phys. Lett.* **2015**, *106*, 221101.
[131] F. Liu, A. J. Brash, J. O'Hara, L. M. P. P. Martins, C. L. Phillips, R. J. Coles, B. Royall, E. Clarke, C. Bentham, N. Prtljaga, I. E. Itskevich, L. R. Wilson, M. S. Skolnick, A. M. Fox, *Nat. Nanotechnol.* **2018**, *13*, 835.
[132] R. Katsumi, Y. Ota, M. Kakuda, S. Iwamoto, Y. Arakawa, *Optica* **2018**, *5*, 691.
[133] M. Gschrey, A. Thoma, P. Schnauber, M. Seifried, R. Schmidt, B. Wohlfeil, L. Kruger, J. H. Schulze, T. Heindel, S. Burger, F. Schmidt, A. Strittmatter, S. Rodt, S. Reitzenstein, *Nat. Commun.* **2015**, *6*, 7662.
[134] A. Thoma, P. Schnauber, M. Gschrey, M. Seifried, J. Wolters, J.-H. Schulze, A. Strittmatter, S. Rodt, A. Carmele, A. Knorr, T. Heindel, S. Reitzenstein, *Phys. Rev. Lett.* **2016**, *116*, 033601.
[135] A. Schlehahn, M. Gaafar, M. Vaupel, M. Gschrey, P. Schnauber, J.-H. Schulze, S. Rodt, A. Strittmatter, W. Stolz, A. Rahimi-Iman, T. Heindel, M. Koch, S. Reitzenstein, *Appl. Phys. Lett.* **2015**, *107*, 041105.
[136] A. Schlehahn, R. Schmidt, C. Hopfmann, J.-H. Schulze, A. Strittmatter, T. Heindel, L. Gantz, E. R. Schmidgall, D. Gershoni, S. Reitzenstein, *Appl. Phys. Lett.* **2016**, *108*, 021104.

[137] T. Heindel, A. Thoma, M. von Helversen, M. Schmidt, A. Schlehahn, M. Gschrey, P. Schnauber, J. H. Schulze, A. Strittmatter, J. Beyer, S. Rodt, A. Carmele, A. Knorr, S. Reitzenstein, *Nat. Commun.* **2017**, *8*, 14870.
[138] A. Thoma, P. Schnauber, J. Böhm, M. Gschrey, J.-H. Schulze, A. Strittmatter, S. Rodt, T. Heindel, S. Reitzenstein, *Appl. Phys. Lett.* **2017**, *110*, 011104.
[139] S. Fischbach, A. Schlehahn, A. Thoma, N. Srocka, T. Gissibl, S. Ristok, S. Thiele, A. Kaganskiy, A. Strittmatter, T. Heindel, S. Rodt, A. Herkommer, H. Giessen, S. Reitzenstein, *ACS Photonics* **2017**, *4*, 1327.
[140] M. Sartison, L. Engel, S. Kolatschek, F. Olbrich, C. Nawrath, S. Hepp, M. Jetter, P. Michler, S. L. Portalupi, *Appl. Phys. Lett.* **2018**, *113*, 032103.
[141] M. Gschrey, F. Gericke, A. Schubler, R. Schmidt, J.-H. Schulze, T. Heindel, S. Rodt, A. Strittmatter, S. Reitzenstein, *Appl. Phys. Lett.* **2013**, *102*, 251113.
[142] J. Claudon, J. Bleuse, N. S. Malik, M. Bazin, P. Jaffrennou, N. Gregersen, C. Sauvan, P. Lalanne, J.-M. Gérard, *Nat. Photonics* **2010**, *4*, 174.
[143] M. Munsch, N. S. Malik, E. Dupuy, A. Delga, J. Bleuse, J.-M. Gérard, J. Claudon, N. Gregersen, J. Mørk, *Phys. Rev. Lett.* **2013**, *110*, 177402.
[144] M. E. Reimer, G. Bulgarini, A. Fognini, R. W. Heeres, B. J. Witek, M. A. M. Versteegh, A. Rubino, T. Braun, M. Kamp, S. Höfling, D. Dalacu, J. Lapointe, P. J. Poole, V. Zwiller, *Phys. Rev. B* **2016**, *93*, 195316.
[145] Y. Chen, I. E. Zadeh, K. D. Jöns, A. Fognini, M. E. Reimer, J. Zhang, D. Dalacu, P. J. Poole, F. Ding, V. Zwiller, O. G. Schmidt, *Appl. Phys. Lett.* **2016**, *108*, 182103.
[146] A. Muller, E. B. Flagg, M. Metcalfe, J. Lawall, G. S. Solomon, *Appl. Phys. Lett.* **2009**, *95*, 173101.
[147] J. Miguel-Sanchez, A. Reinhard, E. Togan, T. Volz, A. Imamoglu, B. Besga, J. Reichel, J. Esteve, *New J. Phys.* **2013**, *15*, 045002.
[148] L. Greuter, S. Starosielec, A. V. Kuhlmann, R. J. Warburton, *Phys. Rev. B* **2015**, *92*, 045302.
[149] D. Najer, M. Renggli, D. Riedel, S. Starosielec, R. J. Warburton, *Appl. Phys. Lett.* **2017**, *110*, 011101.
[150] D. Najer, I. Söllner, P. Sekatski, V. Dolique, M. C. Löbl, D. Riedel, R. Schott, S. Starosielec, S. R. Valentin, A. D. Wieck, N. Sangouard, A. Ludwig, R. J. Warburton, arXiv:1812.08662 (**2018**).
[151] T. Herzog, M. Sartison, S. Kolatschek, S. Hepp, A. Bommer, C. Pauly, F. Mucklich, C. Becher, M. Jetter, S. L. Portalupi, P. Michler, *Quantum Sci. Technol.* **2018**, *3*, 034009.
[152] T. Lund-Hansen, S. Stobbe, B. Julsgaard, H. Thyrrestrup, T. Sünner, M. Kamp, A. Forchel, P. Lodahl, *Phys. Rev. Lett.* **2008**, *101*, 113903.
[153] H. Thyrrestrup, L. Sapienza, P. Lodahl, *Appl. Phys. Lett.* **2010**, *96*, 231106.
[154] A. Schwagmann, S. Kalliakos, I. Farrer, J. P. Griffiths, G. A. C. Jones, D. A. Ritchie, A. J. Shields, *Appl. Phys. Lett.* **2011**, *99*, 261108.
[155] A. Laucht, S. Pütz, T. Günthner, N. Hauke, R. Saive, S. Frédérick, M. Bichler, M.-C. Amann, A. W. Holleitner, M. Kaniber, J. J. Finley, *Phys. Rev. X* **2012**, *2*, 011014.
[156] S. Fattah poor, T. B. Hoang, L. Midolo, C. P. Dietrich, L. H. Li, E. H. Linfield, J. F. P. Schouwenberg, T. Xia, F. M. Pagliano, F. W. M. van Otten, A. Fiore, *Appl. Phys. Lett.* **2013**, *102*, 131105.
[157] M. Arcari, I. Söllner, A. Javadi, S. L. Hansen, S. Mahmoodian, J. Liu, H. Thyrrestrup, E. H. Lee, J. D. Song, S. Stobbe, P. Lodahl, *Phys. Rev. Lett.* **2014**, *113*, 093603.
[158] M. N. Makhonin, J. E. Dixon, R. J. Coles, B. Royall, I. J. Luxmoore, E. Clarke, M. Hugues, M. S. Skolnick, A. M. Fox, *Nano Lett.* **2014**, *14*, 6997.
[159] I. Söllner, S. Mahmoodian, S. L. Hansen, L. Midolo, A. Javadi, G. Kiršanskė, T. Pregnolato, H. El-Ella, E. H. Lee, J. D. Song, S. Stobbe, P. Lodahl, *Nat. Nanotechnol.* **2015**, *10*, 775.
[160] A. Javadi, I. Söllner, M. Arcari, S. L. Hansen, L. Midolo, S. Mahmoodian, G. Kiršanskė, T. Pregnolato, E. H. Lee, J. D. Song, S. Stobbe, P. Lodahl, *Nat. Commun.* **2015**, *6*, 8655.
[161] R. S. Daveau, K. C. Balram, T. Pregnolato, J. Liu, E. H. Lee, J. D. Song, V. Verma, R. Mirin, S. W. Nam, L. Midolo, S. Stobbe, K. Srinivasan, P. Lodahl, *Optica* **2017**, *4*, 178.
[162] G. Kiršanskė, H. Thyrrestrup, R. S. Daveau, C. L. Dreeßen, T. Pregnolato, L. Midolo, P. Tighineanu, A. Javadi, S. Stobbe, R. Schott, A. Ludwig, A. D. Wieck, S. I. Park, J. D. Song, A. V. Kuhlmann, I. Söllner, M. C. Löbl, R. J. Warburton, P. Lodahl, *Phys. Rev. B* **2017**, *96*, 165306.
[163] A. Javadi, D. Ding, M. H. Appel, S. Mahmoodian, M. C. Löbl, I. Söllner, R. Schott, C. Papon, T. Pregnolato, S. Stobbe, L. Midolo, T. Schröder, A. D. Wieck, A. Ludwig, R. J. Warburton, P. Lodahl, *Nat. Nanotechnol.* **2018**, *13*, 398.
[164] X. Zhou, I. Kulkova, T. Lund-Hansen, S. L. Hansen, P. Lodahl, L. Midolo, *Appl. Phys. Lett.* **2018**, *113*, 251103.
[165] H. Thyrrestrup, G. Kiršanskė, H. Le Jeannic, T. Pregnolato, L. Zhai, L. Raahauge, L. Midolo, N. Rotenberg, A. Javadi, R. Schott, A. D. Wieck, A. Ludwig, M. C. Löbl, I. Söllner, R. J. Warburton, P. Lodahl, *Nano Lett.* **2018**, *18*, 1801.
[166] D. Hallett, A. P. Foster, D. L. Hurst, B. Royall, P. Kok, E. Clarke, I. E. Itskevich, A. M. Fox, M. S. Skolnick, L. R. Wilson, *Optica* **2018**, *5*, 644.
[167] S. Mahmoodian, P. Lodahl, A. S. Sørensen, *Phys. Rev. Lett.* **2016**, *117*, 240501.
[168] K. Müller, A. Rundquist, K. A. Fischer, T. Sarmiento, K. G. Lagoudakis, Y. A. Kelaita, C. Sánchez Munoz, E. del Valle, F. P. Laussy, J. Vučković, *Phys. Rev. Lett.* **2015**, *114*, 233601.
[169] K. Müller, K. A. Fischer, A. Rundquist, C. Dory, K. G. Lagoudakis, T. Sarmiento, Y. A. Kelaita, V. Borish, J. Vučković, *Phys. Rev. X* **2015**, *5*, 031006.
[170] D. Englund, A. Faraon, I. Fushman, N. Stoltz, P. Petroff, J. Vučković, *Nature* **2007**, *450*, 857.
[171] A. Faraon, I. Fushman, D. Englund, N. Stoltz, P. Petroff, J. Vučković, *Nat. Phys.* **2008**, *4*, 859.
[172] A. Reinhard, T. Volz, M. Winger, A. Badolato, K. J. Hennessy, E. L. Hu, A. Imamoglu, *Nat. Photonics* **2011**, *6*, 93.
[173] K. A. Fischer, Y. A. Kelaita, N. V. Sapra, C. Dory, K. G. Lagoudakis, K. Müller, J. Vučković, *Phys. Rev. Applied* **2017**, *7*, 044002.
[174] K. A. Fischer, K. Müller, A. Rundquist, T. Sarmiento, A. Y. Piggott, Y. Kelaita, C. Dory, K. G. Lagoudakis, J. Vučković, *Nat. Photon.* **2016**, *10*, 163.
[175] Y. Ota, D. Takamiya, R. Ohta, H. Takagi, N. Kumagai, S. Iwamoto, Y. Arakawa, *Appl. Phys. Lett.* **2018**, *112*, 093101.
[176] K. Fischer, S. Sun, D. Lukin, Y. Kelaita, R. Trivedi, J. Vučković, *Phys. Rev. A* **2018**, *98*, 021802.
[177] B. Hensen, H. Bernien, A. E. Dréau, A. Reiserer, N. Kalb, M. S. Blok, J. Ruitenberg, R. F. L. Vermeulen, R. N. Schouten, C. Abellán, W. Amaya, V. Pruneri, M. W. Mitchell, M. Markham, D. J. Twitchen, D. Elkouss, S. Wehner, T. H. Taminiau, R. Hanson, *Nature* **2015**, *526*, 682.
[178] J. Nilsson, R. M. Stevenson, K. H. A. Chan, J. Skiba-Szymanska, M. Lucamarini, M. B. Ward, A. J. Bennett, C. L. Salter, I. Farrer, D. A. Ritchie, A. J. Shields, *Nat. Photonics* **2013**, *7*, 311.
[179] M. Reindl, D. Huber, C. Schimpf, S. F. C. da Silva, M. B. Rota, H. Huang, V. Zwiller, K. D. Jöns, A. Rastelli, R. Trotta, *Sci. Adv.* **2018**, *4*, eaau1255.
[180] O. Benson, C. Santori, M. Pelton, Y. Yamamoto, *Phys. Rev. Lett.* **2000**, *84*, 2513.
[181] N. Akopian, N. H. Lindner, E. Poem, Y. Berlatzky, J. Avron, D. Gershoni, B. D. Gerardot, P. M. Petroff, *Phys. Rev. Lett.* **2006**, *96*, 130501.
[182] R. Hafenbrak, S. M. Ulrich, P. Michler, L. Wang, A. Rastelli, O. G. Schmidt, *New J. Phys.* **2007**, *9*, 315.

[183] A. Muller, W. Fang, J. Lawall, G. S. Solomon, *Phys. Rev. Lett.* **2009**, *103*, 217402.
[184] A. Dousse, J. Suffczyński, A. Beveratos, O. Krebs, A. Lemaître, I. Sagnes, J. Bloch, P. Voisin, P. Senellart, *Nature* **2010**, *466*, 217.
[185] M. A. M. Versteegh, M. E. Reimer, K. D. Jöns, D. Dalacu, P. J. Poole, A. Gulinatti, A. Giudice, V. Zwiller, *Nat. Commun.* **2014**, *5*, 5298.
[186] M. Müller, S. Bounouar, K. D. Jöns, M. Glässl, P. Michler, *Nat. Photonics* **2014**, *8*, 224.
[187] R. Trotta, J. S. Wildmann, E. Zallo, O. G. Schmidt, A. Rastelli, *Nano Lett.* **2014**, *14*, 3439.
[188] T. Huber, A. Predojević, M. Khoshnegar, D. Dalacu, P. J. Poole, H. Majedi, G. Weihs, *Nano Lett.* **2014**, *14*, 7107.
[189] H. Jayakumar, A. Predojević, T. Kauten, T. Huber, G. S. Solomon, G. Weihs, *Nat. Commun.* **2014**, *5*, 4251.
[190] R. Trotta, J. Martín-Sánchez, I. Daruka, C. Ortix, A. Rastelli, *Phys. Rev. Lett.* **2015**, *114*, 150502.
[191] J. Zhang, J. S. Wildmann, F. Ding, R. Trotta, Y. Huo, E. Zallo, D. Huber, A. Rastelli, O. G. Schmidt, *Nat. Commun.* **2015**, *6*, 10067.
[192] Y. Chen, J. Zhang, M. Zopf, K. Jung, Y. Zhang, R. Keil, F. Ding, O. G. Schmidt, *Nat. Commun.* **2016**, *7*, 10387.
[193] R. Trotta, J. Martín-Sánchez, J. S. Wildmann, G. Piredda, M. Reindl, C. Schimpf, E. Zallo, S. Stroj, J. Edlinger, A. Rastelli, *Nat. Commun.* **2016**, *7*, 10375.
[194] T. Huber, L. Ostermann, M. Prilmüller, G. S. Solomon, H. Ritsch, G. Weihs, A. Predojević, *Phys. Rev. B* **2016**, *93*, 201301.
[195] R. Keil, M. Zopf, Y. Chen, B. Höfer, J. Zhang, F. Ding, O. G. Schmidt, *Nat. Commun.* **2017**, *8*, 15501.
[196] F. Olbrich, J. Höschele, M. Mü'ller, J. Kettler, S. L. Portalupi, M. Paul, M. Jetter, P. Michler, *Appl. Phys. Lett.* **2017**, *111*, 133106.
[197] D. Huber, M. Reindl, Y. Huo, H. Huang, J. S. Wildmann, O. G. Schmidt, A. Rastelli, R. Trotta, *Nat. Commun.* **2017**, *8*, 15506.
[198] K. D. Jöns, L. Schweickert, M. A. M. Versteegh, D. Dalacu, P. J. Poole, A. Gulinatti, A. Giudice, V. Zwiller, M. E. Reimer, *Sci. Rep.* **2017**, *7*, 1700.
[199] J. Zhang, E. Zallo, B. Höfer, Y. Chen, R. Keil, M. Zopf, S. Böttner, F. Ding, O. G. Schmidt, *Nano Lett.* **2017**, *17*, 501.
[200] D. Huber, M. Reindl, S. F. C. da Silva, C. Schimpf, J. Martín-Sánchez, H. Huang, G. Piredda, J. Edlinger, A. Rastelli, R. Trotta, *Phys. Rev. Lett.* **2018**, *121*, 033902.
[201] T. Müller, J. Skiba-Szymanska, A. B. Krysa, J. Huwer, M. Felle, M. Anderson, R. M. Stevenson, J. Heffernan, D. A. Ritchie, A. J. Shields, *Nat. Commun.* **2018**, *9*, 862.
[202] F. B. Basset, S. Bietti, M. Reindl, L. Esposito, A. Fedorov, D. Huber, A. Rastelli, E. Bonera, R. Trotta, S. Sanguinetti, *Nano Lett.* **2018**, *18*, 505.
[203] M. Prilmüller, T. Huber, M. Müller, P. Michler, G. Weihs, A. Predojević, *Phys. Rev. Lett.* **2018**, *121*, 110503.
[204] R. Trotta, E. Zallo, C. Ortix, P. Atkinson, J. D. Plumhof, J. van den Brink, A. Rastelli, O. G. Schmidt, *Phys. Rev. Lett.* **2012**, *109*, 147401.
[205] R. Trotta, P. Atkinson, J. D. Plumhof, E. Zallo, R. O. Rezaev, S. Kumar, S. Baunack, J. R. Schröter, A. Rastelli, O. G. Schmidt, *Adv. Mater.* **2012**, *24*, 2668.
[206] Y. H. Huo, A. Rastelli, O. G. Schmidt, *Appl. Phys. Lett.* **2013**, *102*, 152105.
[207] Y. Chen, M. Zopf, R. Keil, F. Ding, O. G. Schmidt, *Nat. Commun.* **2018**, *9*, 2994.
[208] M. Atatüre, J. Dreiser, A. Badolato, A. Högele, K. Karrai, A. Imamoglu, *Science* **2006**, *312*, 551.
[209] X. Xu, Y. Wu, B. Sun, Q. Huang, J. Cheng, D. G. Steel, A. S. Bracker, D. Gammon, C. Emary, L. J. Sham, *Phys. Rev. Lett.* **2007**, *99*, 097401.
[210] A. J. Ramsay, S. J. Boyle, R. S. Kolodka, J. B. B. Oliveira, J. Skiba-Szymanska, H. Y. Liu, M. Hopkinson, A. M. Fox, M. S. Skolnick, *Phys. Rev. Lett.* **2008**, *100*, 197401.
[211] P.-L. Ardelt, T. Simmet, K. Müller, C. Dory, K. A. Fischer, A. Bechtold, A. Kleinkauf, H. Riedl, J. J. Finley, *Phys. Rev. B* **2015**, *92*, 115306.
[212] K. De Greve, L. Yu, P. L. McMahon, J. S. Pelc, C. M. Natarajan, N. Y. Kim, E. Abe, S. Maier, C. Schneider, M. Kamp, S. Höfling, R. H. Hadfield, A. Forchel, M. M. Fejer, Y. Yamamoto, *Nature* **2012**, *491*, 421.
[213] W. B. Gao, P. Fallahi, E. Togan, J. Miguel-Sanchez, A. Imamoglu, *Nature* **2012**, *491*, 426.
[214] J. R. Schaibley, A. P. Burgers, G. A. McCracken, L.-M. Duan, P. R. Berman, D. G. Steel, A. S. Bracker, D. Gammon, L. J. Sham, *Phys. Rev. Lett.* **2013**, *110*, 167401.
[215] K. De Greve, P. L. McMahon, L. Yu, J. S. Pelc, C. Jones, C. M. Natarajan, N. Y. Kim, E. Abe, S. Maier, C. Schneider, M. Kamp, S. Höfling, R. H. Hadfield, A. Forchel, M. M. Fejer, Y. Yamamoto, *Nat. Commun.* **2013**, *4*, 2228.
[216] W. B. Gao, P. Fallahi, E. Togan, A. Delteil, Y. S. Chin, J. Miguel-Sanchez, A. Imamoğlu, *Nat. Commun.* **2013**, *4*, 2744.
[217] R. Stockill, M. J. Stanley, L. Huthmacher, E. Clarke, M. Hugues, A. J. Miller, C. Matthiesen, C. Le Gall, M. Atatüre, *Phys. Rev. Lett.* **2017**, *119*, 010503.
[218] A. Delteil, Z. Sun, W.-b. Gao, E. Togan, S. Faelt, A. Imamoğlu, *Nat. Phys.* **2015**, *12*, 218.
[219] I. A. Merkulov, A. L. Efros, M. Rosen, *Phys. Rev. B* **2002**, *65*, 205309.
[220] S. I. Erlingsson, Y. V. Nazarov, *Phys. Rev. B* **2004**, *70*, 205327.
[221] M. Kroutvar, Y. Ducommun, D. Heiss, M. Bichler, D. Schuh, G. Abstreiter, J. J. Finley, *Nature* **2004**, *432*, 81.
[222] D. Heiss, S. Schaeck, H. Huebl, M. Bichler, G. Abstreiter, J. J. Finley, D. V. Bulaev, D. Loss, *Phys. Rev. B* **2007**, *76*, 241306.
[223] X. Xu, B. Sun, P. R. Berman, D. G. Steel, A. S. Bracker, D. Gammon, L. J. Sham, *Nat. Phys.* **2008**, *4*, 692.
[224] D. Press, T. D. Ladd, B. Zhang, Y. Yamamoto, *Nature* **2008**, *456*, 218.
[225] D. Press, K. De Greve, P. L. McMahon, T. D. Ladd, B. Friess, C. Schneider, M. Kamp, S. Höfling, A. Forchel, Y. Yamamoto, *Nat. Photonics* **2010**, *4*, 367.
[226] K. De Greve, P. L. McMahon, D. Press, T. D. Ladd, D. Bisping, C. Schneider, M. Kamp, L. Worschech, S. Höfling, A. Forchel, Y. Yamamoto, *Nat. Phys.* **2011**, *7*, 872.
[227] A. V. Kuhlmann, J. Houel, A. Ludwig, L. Greuter, D. Reuter, A. D. Wieck, M. Poggio, R. J. Warburton, *Nat. Phys.* **2013**, *9*, 570.
[228] R. J. Warburton, *Nat. Mater.* **2013**, *12*, 483.
[229] A. Bechtold, D. Rauch, F. Li, T. Simmet, P.-L. Ardelt, A. Regler, K. Müller, N. A. Sinitsyn, J. J. Finley, *Nat. Phys.* **2015**, *11*, 1005.
[230] J. H. Prechtel, A. V. Kuhlmann, J. Houel, A. Ludwig, S. R. Valentin, A. D. Wieck, R. J. Warburton, *Nat. Mater.* **2016**, *15*, 981.
[231] R. Stockill, C. Le Gall, C. Matthiesen, L. Huthmacher, E. Clarke, M. Hugues, M. Atatüre, *Nat. Commun.* **2016**, *7*, 12745.
[232] L. Huthmacher, R. Stockill, E. Clarke, M. Hugues, C. Le Gall, M. Atatüre, *Phys. Rev. B* **2018**, *97*, 241413.
[233] G. Éthier-Majcher, D. Gangloff, R. Stockill, E. Clarke, M. Hugues, C. Le Gall, M. Atatüre, *Phys. Rev. Lett.* **2017**, *119*, 130503.
[234] D. A. Gangloff, G. Éthier-Majcher, C. Lang, E. V. Denning, J. H. Bodey, D. M. Jackson, E. Clarke, M. Hugues, C. Le Gall, M. Atatüre, *Science* **2019**, *364*, 62.
[235] R. Raussendorf, D. E. Browne, H. J. Briegel, *Phys. Rev. A* **2003**, *68*, 022312.
[236] D. Scerri, R. N. E. Malein, B. D. Gerardot, E. M. Gauger, *Phys. Rev. A* **2018**, *98*, 022318.
[237] M. A. Nielsen, *Phys. Rev. Lett.* **2004**, *93*, 040503.
[238] R. Prevedel, P. Walther, F. Tiefenbacher, P. Böhi, R. Kaltenbaek, T. Jennewein, A. Zeilinger, *Nature* **2007**, *445*, 65.
[239] M. A. Nielsen, I. Chuang, *Quantum Computation and Quantum Information*, Cambridge University Press, Cambridge, MA **2002**.

[240] H.-J. Briegel, W. Dür, J. I. Cirac, P. Zoller, *Phys. Rev. Lett.* **1998**, *81*, 5932.
[241] N. H. Lindner, T. Rudolph, *Phys. Rev. Lett.* **2009**, *103*, 113602.
[242] S. E. Economou, N. Lindner, T. Rudolph, *Phys. Rev. Lett.* **2010**, *105*, 093601.
[243] E. A. Stinaff, M. Scheibner, A. S. Bracker, I. V. Ponomarev, V. L. Korenev, M. E. Ware, M. F. Doty, T. L. Reinecke, D. Gammon, *Science* **2006**, *311*, 636.
[244] M. Van den Nest, J. Dehaene, B. De Moor, *Phys. Rev. A* **2004**, *69*, 022316.
[245] D. Buterakos, E. Barnes, S. E. Economou, *Phys. Rev. X* **2017**, *7*, 041023.
[246] A. Russo, E. Barnes, S. E. Economou, arXiv:1811.06305, **2018**.
[247] I. Schwartz, D. Cogan, E. R. Schmidgall, Y. Don, L. Gantz, O. Kenneth, N. H. Lindner, D. Gershoni, *Science* **2016**, *354*, 434.
[248] D. P. McCutcheon, N. H. Lindner, T. Rudolph, *Phys. Rev. Lett.* **2014**, *113*, 260503.
[249] I. Schwarz, T. Rudolph, *Phys. Rev. A* **2012**, *85*, 050306.
[250] T. Nutz, A. Milne, P. Shadbolt, T. Rudolph, *APL Photonics* **2017**, *2*, 066103.
[251] M. E. Peskin, D. V. Schroeder, *An Introduction To Quantum Field Theory*, Westview Press, Boulder, CO, **1995**.
[252] R. Trivedi, K. Fischer, S. D. Mishra, J. Vučković, *Phys. Rev. B* **2019**, *100*, 043827.